Non-Schmid Effects on the Behavior of Polycrystals—with Applications to Ni_3Al

MING DAO, BING JEAN LEE, and ROBERT J. ASARO

The elastoviscoplastic single crystal constitutive model incorporating *non-Schmid effects* developed by Dao and Asaro (Mater. Sci. Eng. A, 1993, vol. 170, pp. 143-60) is introduced into Asaro and Needleman's (Acta Metall., 1985, vol. 33, pp. 923-53) Taylor-like polycrystal model as well as Harren and Asaro's (J. Mech. Phys. Solids, 1989, vol. 37, pp. 191-232) finite element polycrystal model. The single crystal non-Schmid effects, strain hardening, latent hardening, and rate sensitivity, are all described on the individual slip system level, while polycrystal mechanical properties on macroscale are predicted. In general, it is found that non-Schmid effects can have important influences on the "constant offset plastic strain yield surfaces," stress-strain behavior, texture development, and shear band formation. Finite element calculations show that with moderate non-Schmid effects, localized deformation within a polycrystal aggregate tends to initiate earlier and form sharper and more intense shear bands. Heavy shear banding is found to produce less pronounced textures, which is consistent with existing experimental evidence on Ni_3Al. Examples with Ni_3Al demonstrate that the kind of non-Schmid effects existing in Ni_3Al can increase the generalized Taylor factor to values much higher than 3.06, raise the polycrystal strain hardening rate much higher than that which would be obtained using Schmid's rule, and influence the deformation texture.

I. INTRODUCTION

FOR single crystals, Schmid's rule states that yielding occurs on a slip system when the resolved shear stress *alone* reaches a critical value. While the Schmid rule is often a good approximation for simple metals, deviations from it are inevitable. Such deviations are here termed *non-Schmid effects*. For example, significant deviations from Schmid's rule have been reported for Zn single crystals,[4] for intermetallics such as Ni_3Ga,[5] Ni_3Al,[6] and Ti_3Al (DO_{19})[7] single crystals, and for quasisingle crystalline high density polyethylene[8] polymers.

The prevailing theory of single crystal plasticity is based on the pioneering work of Taylor[9,10] and the more recent work of Hill and Rice.[11] The influence of non-Schmid effects on ductile single crystals was first rigorously formulated within a rate-independent framework by Asaro and Rice.[12] Asaro and Rice recognized that under a single slip mode, non-Schmid effects are essential to initiate shear bands for crystals undergoing positive strain hardening. Using a double symmetric slip model and within the framework of Schmid's rule, Asaro[13] pointed out that localized shearing is possible for crystals undergoing multiple slip with positive strain hardening. Peirce *et al.*[14] later extended this formulation into a finite strain elastoviscoplastic framework. Recently, Dao and Asaro[1] developed a finite strain elastoviscoplastic multiple slip theory incorporating non-Schmid effects, based on the aforementioned earlier works. Qin and Bassani,[15,16] within a rate-independent framework, also developed a multiple slip theory using non-Schmid effects based on the earlier work of Asaro and Rice.

Parallel to the development of single crystal plasticity theory, polycrystalline averaging schemes have advanced significantly since the early work of Taylor.[9,10] A few important advances along this line are the following. Hill[17] proposed a self-consistent small-strain elastoplastic rate-independent model; Hutchinson[18] applied Hill's model and calculated a stress-strain response within the context of small strains for single phase fcc polycrystals; Iwakuma and Nemat-Nasser[19] and Nemat-Nasser and Obata[20] modified Hill's framework for finite strains and two-dimensional (2-D) calculations were performed; Asaro and Needleman[2] developed a finite-strain elastoviscoplastic Taylor-like model where full three-dimensional (3-D) calculations were made; Molinari *et al.*[21] used a self-consistent scheme to calculate the viscoplastic response of polycrystals in three dimensions; Harren[22,23] used the elastoviscoplastic self-consistent framework of Nemat-Nasser and Obata and extended it into three dimensions, where results were found similar to those obtained by Asaro and Needleman's[2] Taylor-like model; and, recently, 2-D and 3-D finite element calculations were carried out by Harren and Asaro[3] and later by Mathur and Dawson[25] and Kalidindi *et al.*,[24] respectively. In general, Taylor-like models predict sharper textures than the self-consistent and finite element models,[3,21,24] although all three types of models give fairly good predictions of texture and stress-strain response as compared against experiments, at least for fcc polycrystals.[2,21,24] Nevertheless, to the best of our knowledge, the previous efforts of the crystal plasticity in polycrystals to date have been based on the Schmid rule.

It is clear that non-Schmid effects can affect the single crystal's mechanical behavior, *i.e.*, flow stress[4,5,26] and critical conditions of localization.[1,12,27] How a polycrystal aggregate's mechanical behavior is influenced by the non-Schmid effects of its constituent single crystals is still

MING DAO, Postdoctoral Research Engineer, and ROBERT J. ASARO, Professor, are with the Department of Applied Mechanics and Engineering Sciences, University of California–San Diego, La Jolla, CA 92093-0411. BING JEAN LEE, Associate Professor, is with the Department of Civil Engineering, Feng Chia University, Taichung, Taiwan, Republic of China.

Manuscript submitted February 9, 1995.

an outstanding question. The objective of this study, therefore, has been to explore the general influences of non-Schmid effects on the initial yielding, stress-strain behavior, texture development, and localized deformation in polycrystals.

The outline of this article is as follows. In Section II–A, the single crystal constitutive theory is presented. Section II–B–1 briefly describes the 3-D Taylor-like polycrystal model used, and Section II–B–2 introduces an idealized finite element polycrystal model. Section III–A reviews the non-Schmid factors in some simple metals as well as intermetallics. Sections II–B through III–E describe the general influences of non-Schmid effects on initial yielding, stress-strain behavior, texture development, and localized deformation, respectively. Section III–F provides several applications toward polycrystalline Ni_3Al. Finally, a discussion and conclusions are given in Section IV.

II. THEORY

A. *Single Crystal Constitutive Model*

The constitutive theory used in the analyses is a rate-dependent crystal plasticity theory incorporating non-Schmid effects described by Dao and Asaro.[1] The theory is developed from earlier versions by Asaro and Rice,[12] Asaro,[13] Peirce *et al.*,[14,28] and most recently McHugh *et al.*[29] The deformation of a single crystal from the reference configuration to the current configuration can be decomposed into plastic shearing, thermal deformation due to temperature change, elastic stretching, and lattice rotation. The deformation gradient, $\mathbf{F}$, is thus decomposed as

$$\mathbf{F} = \mathbf{F}^* \cdot \mathbf{F}^\theta \cdot \mathbf{F}^P \qquad [1]$$

where $\mathbf{F}^P$ is the plastic deformation gradient which represents the shear flow of crystal through the undeformed lattice along various slip systems, $\mathbf{F}^\theta$ is the thermal deformation gradient which represents the deformation of the crystal due to temperature change, and $\mathbf{F}^*$ is the elastic deformation gradient which represents the elastic stretching and rigid body rotation of the crystal. The velocity gradient of the single crystal can be defined as

$$\mathbf{L} = \dot{\mathbf{F}} \cdot \mathbf{F}^{-1} \qquad [2]$$

and when the decomposition [1] is used, it becomes

$$\mathbf{L} = \dot{\mathbf{F}}^* \cdot \mathbf{F}^{*-1} + \mathbf{F}^* \cdot \dot{\mathbf{F}}^\theta \cdot \mathbf{F}^{\theta-1} \cdot \mathbf{F}^{*-1} + \mathbf{F}^* \cdot \mathbf{F}^\theta \cdot \dot{\mathbf{F}}^P \cdot \mathbf{F}^{P-1} \cdot \mathbf{F}^{\theta-1} \cdot \mathbf{F}^{*-1} \qquad [3]$$

The velocity gradients of plastic shear flow can be written as

$$\dot{\mathbf{F}}^P \cdot \mathbf{F}^{P-1} = \dot{\gamma}_\alpha \mathbf{s}_\alpha \mathbf{m}_{(\alpha)} \qquad [4]$$

where $\dot{\gamma}_\alpha$ is the shear rate on the α slip system of which the α slip system is defined by its slip direction $\mathbf{s}_\alpha$ and its slip plane normal $\mathbf{m}_\alpha$. The velocity gradient due to thermal deformation can be written as

$$\dot{\mathbf{F}}^\theta \cdot \mathbf{F}^{\theta-1} = \dot{\theta}\boldsymbol{\alpha} \qquad [5]$$

where $\dot{\theta}$ is the rate of change of temperature and $\boldsymbol{\alpha}$ is the thermal expansion tensor which is, for example, diagonal for cubic crystals if the reference Cartesian base vectors align with the cubic crystal axes.

To account for the non-Schmid effects, the shear rate on the slip system α, $\dot{\gamma}_\alpha$, in Eq. [4] is taken to be in the following form:

$$\dot{\gamma}_\alpha = \dot{\gamma}_0 \operatorname{sgn}\{\tau_\alpha\} \left\{ \left| \frac{\tau^D_{(\alpha)}}{g_{(\alpha)}} \right| \right\}^{1/m} \qquad [6]$$

where τ_α is the current value of the resolved shear stress, τ^D_α is the *loading parameter* for slip system α defined further subsequently, $g_\alpha > 0$ is the current value of the slip resistance, m is the material rate sensitivity exponent (which will be taken the same for all slip systems), and $\dot{\gamma}_0$ is a reference shear rate.

The loading parameter to the slip system α, τ^D_α, is given as

$$\tau^D_\alpha = \tau_\alpha + \boldsymbol{\eta}_\alpha : \boldsymbol{\tau} = \mathbf{m}^*_\alpha \cdot \boldsymbol{\tau} \cdot \mathbf{s}^*_\alpha + \boldsymbol{\eta}_\alpha : \boldsymbol{\tau} \qquad [7]$$

where

$$\mathbf{s}^*_\alpha = \mathbf{F}^* \cdot \mathbf{F}^\theta \cdot \mathbf{s}_\alpha;\ \mathbf{m}^*_\alpha = \mathbf{m}_\alpha \cdot \mathbf{F}^{\theta-1} \cdot \mathbf{F}^{*-1};\ \mathbf{z}^*_\alpha = \mathbf{s}^*_\alpha \times \mathbf{m}^*_\alpha;\ \boldsymbol{\tau} = J\boldsymbol{\sigma} \qquad [8]$$

in which $J = \det\{\mathbf{F}\}$ is the Jacobian, $\boldsymbol{\tau}$ is the Kirchhoff stress tensor, $\boldsymbol{\sigma}$ is the Cauchy stress tensor, $\mathbf{s}^*_\alpha$ is along the α slip direction in the current configuration, $\mathbf{m}^*_\alpha$ is normal to the α slip plane, $\mathbf{z}^*_\alpha$ is normal to both $\mathbf{s}^*_\alpha$ and $\mathbf{m}^*_\alpha$, and $\boldsymbol{\eta}_\alpha$ is the tensor of non-Schmid effects for slip system α which, when aligned with $\mathbf{s}^*_\alpha$, $\mathbf{m}^*_\alpha$, and $\mathbf{z}^*_\alpha$, takes the simple form

$$\boldsymbol{\eta} = \begin{pmatrix} \eta_{ss} & 0 & \eta_{sz} \\ 0 & \eta_{mm} & \eta_{mz} \\ \eta_{sz} & \eta_{mz} & \eta_{zz} \end{pmatrix} \qquad [9]$$

The slip resistance g_α is obtained by the path dependent integration of the evolution equation

$$\dot{g}_\alpha = h_{\alpha\beta}(\gamma_\alpha)\,|\dot{\gamma}_\beta| + g^\theta_\alpha\,\dot{\theta},\ \gamma_a = \int_0^t \sum_\alpha |\dot{\gamma}_\alpha|\,dt \qquad [10]$$

where $h_{\alpha\beta}$ is a matrix of hardening moduli, g^θ_α is the rate of change of slip resistance with respect to temperature alone, and γ_a is the accumulated sum of slips. The initial conditions for this evolution are given by $g_\alpha(\gamma_a = 0, \theta = \theta_0) = g^0_\alpha(\theta_0)$, where θ_0 is a reference temperature. The specific form of the hardening matrix is taken as

$$h_{\alpha\beta} = qh + (1 - q)\,h\delta_{\alpha\beta} \qquad [11]$$

where q sets the level of latent hardening to the self-hardening of the slip system and h is the self-hardening rate. Other forms of the latent hardening relations may be used, in particular, those recently developed by Wu *et al.*[30] and Bassani and Wu.[31]

The single crystal's constitutive description is completed with a specification of its elasticity. Here, we consider the elastic anisotropy of the single crystal and assume the following form:

$$\dot{\mathbf{S}}^* = \mathbf{K} : \dot{\mathbf{E}}^* \qquad [12]$$

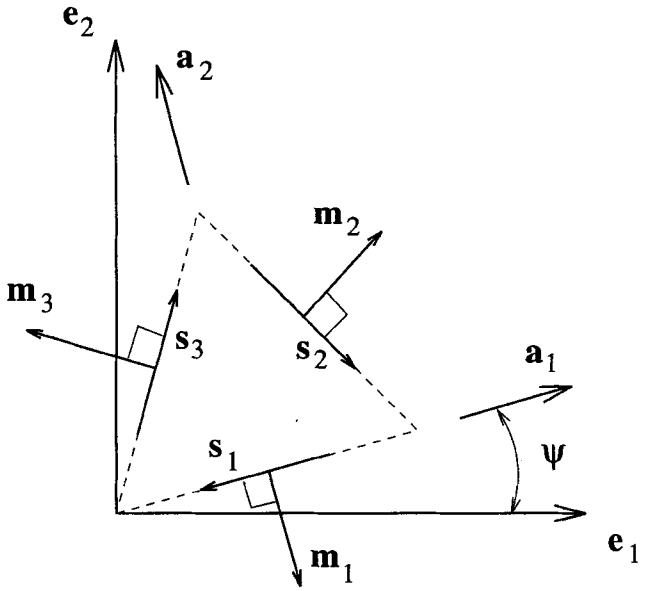

Fig. 1—2-D single crystal slip geometry used in the idealized polycrystal model. The three slip systems are arranged in an equilateral triangle, and the reference laboratory base vectors $\mathbf{e}_i$ are at an angle ψ with respect to reference crystal base vectors $\mathbf{a}_i$.

where $\mathbf{S}^* = \mathbf{F}^{*-1} \cdot \boldsymbol{\tau} \cdot \mathbf{F}^{*-T}$ is the lattice-based second Piola–Kirchhoff stress, $\mathbf{E}^* = 1/2\ (\mathbf{F}^{*T} \cdot \mathbf{F}^* - \mathbf{I})$ is the Green strain of the lattice, and $\mathbf{I}$ is the second-order identity tensor. The final constitutive theory is then expressed in terms of the second Piola–Kirchhoff stress, $\mathbf{S} = \mathbf{F}^{-1} \cdot \boldsymbol{\tau} \cdot \mathbf{F}^{-T}$, and the Green strain, $\mathbf{E} = 1/2(\mathbf{F}^T \cdot \mathbf{F} - \mathbf{I})$. Straightforward manipulation of the preceding equations gives the rate form of the governing constitutive equation, *viz.*

$$\dot{\mathbf{S}} = \mathbf{L} : \dot{\mathbf{E}} - \dot{\gamma}_\alpha \mathbf{X}_\alpha - \dot{\theta}\mathbf{Y} \qquad [13]$$

where

$$\mathbf{L}_{ijrn} = \hat{\mathbf{F}}^{-1}_{ik}\, \hat{\mathbf{F}}^{-1}_{jl}\, \mathbf{K}_{klpq}\, \hat{\mathbf{F}}^{-1}_{rp}\, \hat{\mathbf{F}}^{-1}_{nq}$$

$$\begin{aligned}
&\hat{\mathbf{F}} = \mathbf{F}^\theta \cdot \mathbf{F}^P \\
&\mathbf{X}_\alpha = \hat{\mathbf{F}}^{-1} \cdot \{\mathbf{K} : \mathbf{A}_\alpha + 2\mathbf{H}_\alpha\} \cdot \hat{\mathbf{F}}^{-T} \\
&\mathbf{Y} = \hat{\mathbf{F}}^{-1} \cdot \{\mathbf{K} : \mathbf{B} + 2\mathbf{Q}\} \cdot \hat{\mathbf{F}}^{-T} \\
&\mathbf{A}_\alpha = \text{sym}\ \{\mathbf{F}^{*T} \cdot \mathbf{F}^* \cdot \mathbf{F}^\theta \cdot \{\mathbf{s}_\alpha\, \mathbf{m}_{(\alpha)}\} \cdot \mathbf{F}^{\theta-1}\} \\
&\mathbf{H}_\alpha = \text{sym}\ \{\mathbf{F}^\theta \cdot \{\mathbf{s}_\alpha\, \mathbf{m}_{(\alpha)}\} \cdot \mathbf{F}^{\theta-1} \cdot \mathbf{s}^*\} \\
&\mathbf{B} = \text{sym}\ \{\mathbf{F}^{*T} \cdot \mathbf{F}^* \cdot \boldsymbol{\alpha}\}; \quad \mathbf{Q} = \text{sym}\ \{\boldsymbol{\alpha} \cdot \mathbf{S}^*\}
\end{aligned} \qquad [14]$$

where sym $\{\cdot\}$ means the symmetric part of $\{\cdot\}$. The details of the derivation of Eqs. [13] and [14] may be found elsewhere (*e.g.*, Dève *et al.*[32] and McHugh *et al.*[29]) and are omitted here. It is also useful to rewrite the rate form (Eq. [13]) in terms of the nominal stress $\mathbf{n} = \mathbf{F}^{-1} \cdot \boldsymbol{\tau} = \mathbf{S} \cdot \mathbf{F}^T$. Substituting $\dot{n} = \dot{\mathbf{S}} \cdot \mathbf{F}^T + \mathbf{S} \cdot \dot{\mathbf{F}}^T$ into Eq. [13] yields

$$\dot{\mathbf{n}} = \mathbf{M} : \dot{\mathbf{F}} - \dot{\gamma}_\alpha \mathbf{R}_\alpha - \dot{\theta}\mathbf{G} \qquad [15]$$

where

$$\begin{aligned}
\mathbf{M}_{ijkl} &= \hat{\mathbf{F}}^{-1}_{ia} \mathbf{F}^*_{jb}\, \mathbf{K}_{abcd}\, \hat{\mathbf{F}}^{-1}_{kc} \mathbf{F}^*_{ld} + \mathbf{S}_{ik}\, \delta_{jl} \\
\mathbf{R}_\alpha &= \mathbf{X}_\alpha \cdot \mathbf{F}^T;\ \mathbf{G} = \mathbf{Y} \cdot \mathbf{F}^T
\end{aligned} \qquad [16]$$

B. *Polycrystal Formulation*

1. *Taylor-like model*

To predict the global response of the polycrystal, the transition from the microresponse of the individual grains to the macroresponse of the polycrystalline aggregate, Asaro and Needleman[2] extended the original model of Taylor,[9,10] in which the deformation gradient within each grain is assumed to be uniform throughout the aggregate, to the finite strain elastic-plastic deformation. In this extended Taylor-like model, compatibility is satisfied and equilibrium holds within each grain, but the intergranular equilibrium is usually violated. This simple averaging procedure gives the macroscopic average nominal stress, $\bar{\mathbf{n}}$, in the polycrystal as the volume average of the nominal stress in each grain, $\mathbf{n}$:

$$\bar{\mathbf{n}} = \langle \mathbf{n} \rangle \qquad [17]$$

where $\langle \cdot \rangle$ indicates the volume average over the aggregate. Note that due to the assumption of homogeneous deformation, the local deformation gradient is constant for each grain (*i.e.*, $\mathbf{F} = \bar{\mathbf{F}}$), which indicates that $\bar{\mathbf{n}}$ and $\dot{\bar{\mathbf{F}}}$ are conjugate variables (*i.e.*, $\langle \mathbf{n} : \dot{\mathbf{F}} \rangle = \bar{\mathbf{n}} : \dot{\bar{\mathbf{F}}}$).

The rate constitutive Eq. [15] can be implemented numerically *via* the one-step, explicit rate tangent method of Peirce *et al.*[14] and has the form

$$\dot{\mathbf{n}}^t = \mathbf{M}^{\tan} : \dot{\mathbf{F}}^t - \dot{\mathbf{R}}^{\tan} - \dot{\mathbf{G}}^{\tan} \qquad [18]$$

where $\mathbf{M}^{\tan}$, $\dot{\mathbf{R}}^{\tan}$, and $\dot{\mathbf{G}}^{\tan}$ are determined explicitly from the state at time t. Taking the volume average over the aggregate, we obtain

$$\dot{\bar{\mathbf{n}}}^t = \bar{\mathbf{M}}^{\tan} : \dot{\bar{\mathbf{F}}}^t - \dot{\bar{\mathbf{R}}}^{\tan} - \dot{\bar{\mathbf{G}}}^{\tan} \qquad [19]$$

which is the macroscopic (time-discrete) constitutive equation for polycrystal. A well-posed rate boundary value problem in terms of $\dot{\bar{\mathbf{n}}}$ and $\dot{\bar{\mathbf{F}}}$ is prescribed for this macroscopic constitutive equation which allows one to solve the rest of the unknown components of $\dot{\bar{\mathbf{n}}}$ and $\dot{\bar{\mathbf{F}}}$. Predictions from the Taylor-like model of Asaro and Needleman[2] concerning the initial yield surfaces, stress-strain curves, and evolution of textures of fcc polycrystals have compared well against the existing experiments on copper. In the current investigation, this Taylor-like model proposed by Asaro and Needleman is employed (with some minor modifications) to study the non-Schmid effects on the behavior of polycrystals with fcc type slip systems. Further details of the model can be found in Reference 2 and are omitted here.

2. *Finite element model*

The 2-D idealization used here was introduced by Harren *et al.*,[33] Harren and Asaro,[3] and McHugh *et al.*[29] for fcc or bcc polycrystals and their metal matrix composites. The 2-D single crystal slip geometry is shown in Figure 1. The three slip systems are arranged in an equilateral triangle, and the reference laboratory base vectors $\mathbf{e}_i$ are at an angle ψ with respect to reference crystal base vectors $\mathbf{a}_i$. The slip directions in this model geometry, $\mathbf{s}_1$, $\mathbf{s}_2$, and $\mathbf{s}_3$, represent the close packed directions of an assemblage of close packed circular cylinders. Note that in a 2-D model, two independent slip systems can accommodate an arbitrary increment of plastic strain, whereas in this model, there are three independent slip systems so that, in a sense, this model resembles the redundancy exhibited by both fcc and bcc polycrystals. Thus, we expect that the qualitative behavior predicted by this model polycrystal will be very

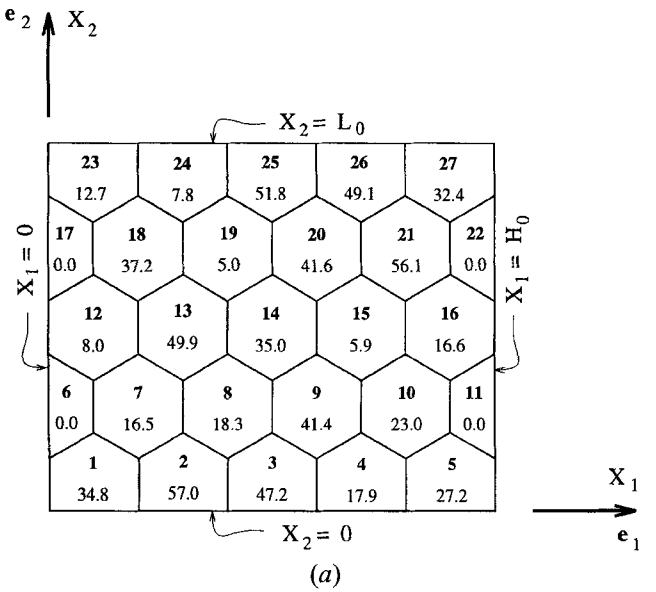

(a)

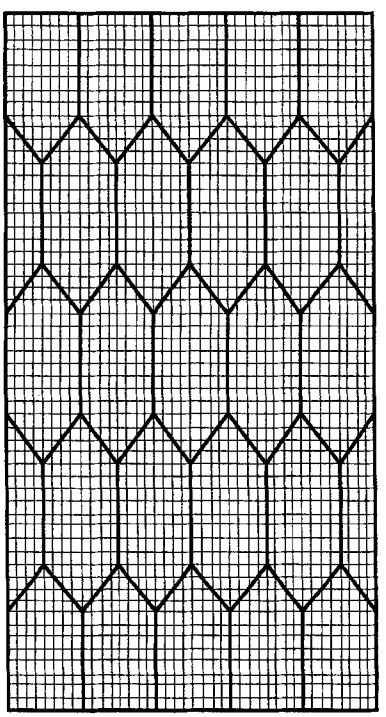

(b)

Fig. 2—(*a*) Reference geometry of the idealized polycrystal model. For each of the 27 grains, the grain number and the grain's initial orientation (in degrees) are shown. (*b*) The finite element mesh used in the polycrystal calculations. The initial mesh consists of rectangular crossed-triangle quadrilateral elements in a uniform grid 40 rectangles wide by 56 rectangles high.

much like simple metals and intermetallics with more than five independent slip systems in three dimensions.

The reference configuration of the polycrystal model is shown in Figure 2(a), where the Cartesian base vectors $\mathbf{e}_i$ describe the orientation of the polycrystal's reference configuration with respect to the laboratory. Each of the 27 grains indicated in Figure 2(a) is defined by an orthogonal transformation $\mathbf{a}_i^n = \psi_{ij}(\psi^n)\mathbf{e}_j$, $n = 1, \ldots, 27$, where ψ^n is the angle ψ shown in Figure 1 for the nth grain. Since a symmetry operation for each grain is a 60 deg rotation about the $\mathbf{e}_3$ axis, a random value between 0 and 60 deg was assigned to each grain with respect to $\mathbf{e}_3$, except for $n = 6$, 11, 17, and 22; for these grains, $\psi = 0$ deg, as explained next. The model polycrystal shown in Figure 2(a) is intended to model a representative group of random oriented grains in a large aggregate compromising many similar groups. Thus, it is desired to subject this group of grains to a plain strain tension or compression mode that would display orthotropic symmetry. Therefore, the material faces $X_1 = H_0$ and $X_2 = 0$ are prescribed as planes of mirror symmetry for the polycrystal model. The complete polycrystal model then is constructed by reflecting the group of grains in Figure 2(a) across the plane $X_1 = H_0$ and then reflecting the two quadrants so produced across the plane $X_2 = 0$. This explains the choice of $\psi = 0$ deg for the four grains, since any other choice would result in misorientations across the boundaries of these "half grains."

The finite element mesh used in the polycrystal calculations consisted initially of rectangular "crossed-triangle" quadrilateral elements in a uniform grid 40 rectangles wide by 56 rectangles high, which is 8960 constant strain triangles totally (Figure 2(b)). The initial width to height ratio of each quadrilateral element is taken as 0.75. This initial ratio is chosen so that the diagonals of the quadrilateral elements will be, more or less, aligned with the microscopic shear bands that are expected to form, as discussed by Harren *et al.*[33] No geometric imperfections were present in the initial mesh. The mesh dimensions were chosen to represent equiaxed grains. Finally, all of the grain boundaries in this polycrystal model coincide with either an edge or a diagonal of a quadrilateral element, *i.e.*, with an edge of a constant strain triangle. As discussed by Harren *et al.*, the grain boundaries are "continuum grain boundaries." This is a continuum theory, and the polycrystal's initial reference configuration is assumed to be stress free and without any lattice perturbations. In fact, each grain boundary is a line across which the initial lattice orientation ψ^n has a jump.

Due to the symmetries of the globally orthotropic deformation mode, only one-fourth of the complete polycrystal structure needs to be analyzed numerically, which is the quadrant depicted in Figure 2. For the simple tension or compression tests, we have the boundary conditions set to be

$$\begin{aligned} \dot{u}_2(X_1, 0) &= 0, \quad & \dot{t}_1(X_1, 0) &= 0 \\ \dot{u}_1(0, X_2) &= 0, \quad & \dot{t}_2(0, X_2) &= 0 \\ \dot{u}_1(H_0, X_2) &= \dot{U}_1, \quad & \dot{t}_2(H_0, X_2) &= 0 \\ \dot{u}_2(X_1, L_0) &= \dot{U}_2, \quad & \dot{t}_1(X_1, L_0) &= 0 \end{aligned} \qquad [20]$$

Here, $\dot{\mathbf{u}} = \dot{u}_i\mathbf{e}_i$ is the material particle velocity; $\dot{\mathbf{t}} = \dot{t}_i e_i$ is the rate of nominal traction, *i.e.*, $\dot{\mathbf{t}} = \dot{\hat{\mathbf{N}}} \cdot \dot{\mathbf{n}}$ ($\hat{\mathbf{N}}$ is the outward unit normal to the aggregate boundaries); $\dot{U}_1$ is the normal velocity on the material face $X_1 = H_0$; and $\dot{U}_2$ is the normal velocity on the material face $X_2 = L_0$. Also, the total loads on the unit cell (polycrystal aggregate) in X_1 and X_2 directions are, respectively,

$$P_1 = \int_0^{L_0} t_1(H_0, X_2)\, dX_2 \text{ and } P_2 = \int_0^{H_0} t_2(X_1, L_0)\, dX_1 \qquad [21]$$

The prescription for boundary value problem is completed

Table I. Non-Schmid Factors for Some Simple Metals

	Zn*	Al-Cu**	Steel (Martensitic)†	Cross-Slip Model‡
η_{sz}	—	0.044	—	0.03 to 0.1
η_{mz}	—	—	—	0.005 to 0.03
η_{ss}	—	—	0.018 to 0.025	—
η_{mm}	~0.1	—	0.018 to 0.025	—
η_{zz}	—	—	0.018 to 0.025	—

*Data from Barendreght and Sharpe.[4]
**Data from Chang and Asaro.[34]
†Data from Spitzig *et al.*[36]
‡Theoretical results from Asaro and Rice.[12]

by setting $\dot{P}_1 = 0$ and $(\dot{U}_2/L_0) = \dot{a}$ for tension or $(\dot{U}_2/L_0) = -\dot{a}$ for compression, and hence, $\dot{U}_1$ and $\dot{P}_2$ are unknowns to be solved during the course of the solution of the rate boundary value problem. The initial state of this problem corresponds to zero stress and zero strain.

III. INFLUENCE OF NON-SCHMID EFFECTS

In order to investigate non-Schmid effects on the behavior of polycrystals, we will first review and estimate the non-Schmid factors in simple metals and intermetallics. Then the contributions of different non-Schmid effects toward the yield surface, stress-strain behavior, texture development, and localization will be explored. After that, several examples are given on the behavior of Ni_3Al polycrystals, where non-Schmid factors of Ni_3Al single crystals have been estimated by Dao and Asaro.[1]

A. *Non-Schmid Effects in Simple Metals and Intermetallics*

1. *Estimation of non-Schmid factors in simple metals*

Asaro and Rice,[12] Chang and Asaro,[34] and Asaro[35] have given some estimated non-Schmid factors for simple metals. Barendreght and Sharpe[4] found in Zn single crystals that η_{mm} could be as high as 0.17. Spitzig *et al.*[36] reported the *strength differential* (SD) to be as high as 0.07 to 0.1 in high strength martensitic steels. The SD is defined as the ratio $(\sigma_c - \sigma_t)/[(\sigma_c + \sigma_t)/2]$, where σ_c and σ_t are yield strengths in uniaxial compression and uniaxial tension, respectively. As pointed out by Asaro and Rice,[12] the strength differential can be expressed as

$$\text{SD} = \frac{4\kappa}{3} \qquad [22]$$

where κ is the pressure sensitivity factor. If $\eta_{ss} = \eta_{mm} = \eta_{zz} = \kappa/3$, their values are estimated to be

$$\eta_{ss} = \eta_{mm} = \eta_{zz} = \frac{1}{4}\,\text{SD} \qquad [23]$$

Estimations and observations of non-Schmid factors for several materials are summarized in Table I.

2. *Estimation of non-Schmid factors in Ni_3Al*

Dao and Asaro[1] have estimated the non-Schmid factors for Ni_3Al at several different temperatures (Table II). These estimated non-Schmid factors can catch the orientation and temperature dependence of single crystalline Ni_3Al, as described by Paidar, Pope, and Vitek (PPV).[26]

3. *Discussion on stress state dependent flow*

To better understand the stress state dependent yielding and plastic flow, we examine the rate-independent limit of the flow rule (Eq. [6]), *viz.*

$$\tau^D_\alpha = g_\alpha \text{ or } \tau_\alpha + \boldsymbol{\eta}_\alpha : \boldsymbol{\tau} = g_\alpha \qquad [24]$$

Here, the yield function g_α is defined as the critical resolved shear stress when τ_α is the only nonzero stress component under the $\mathbf{s}^*_\alpha$, $\mathbf{m}^*_\alpha$, $\mathbf{z}^*_\alpha$ coordinate system. Note that unlike the critical resolved shear stress, g_α so defined is stress state independent and can be readily determined experimentally. The hardening function $h_{\alpha\beta}$ described by Eq. [10] is thus also stress state independent at the current time t, although the path-dependent function $h_{\alpha\beta}$ can be strongly influenced by the loading and orientation histories of the crystal. It is clear that assuming single slip, our definition naturally leads to the same orientation dependence for yielding (τ_α) and hardening $(\partial\tau_\alpha/\partial\gamma_\alpha)$ which was observed for Ni_3Al single crystals below the octahedral slip to cubic slip transition temperature by Aoki and Izumi.[6]

B. *Initial Yield Surface*

While it is clear that the existence of non-Schmid effects can affect the yielding of single crystals, how non-Schmid effects influence the polycrystal yielding behavior remains an outstanding question. On the one hand, if non-Schmid effects exist within each constituent single crystal (or grain), the critical resolved shear stress of each slip system will be orientation dependent (or, more accurately, stress state dependent); on the other hand, the random distribution of grain orientations may average out some of the local orientation dependence.

To study the influence of non-Schmid effects on the constitutive response of the polycrystal aggregate, a set of constant offset effective plastic strain "yield surface" calculations were carried out using the method first introduced by Asaro and Needleman.[2] With $\mathbf{D}$ as the rate of deformation tensor, the Mises effective stress and Mises effective strain are then defined as

$$\sigma_e = \sqrt{\frac{3}{2}\,\sigma'_{ij}\,\sigma'_{ij}} \text{ and } \varepsilon_e = \int_0^t \sqrt{\frac{2}{3}\,D'_{ij}\,D'_{ij}}\,dt \qquad [25]$$

where $(\cdot)'$ denotes deviatoric quantities, *e.g.*,

$$\sigma'_{ij} = \sigma_{ij} - \frac{1}{3}\,\sigma_{kk}\,\delta_{ij}$$

At various stages in each loading history, the polycrystal aggregate is unloaded to a state of zero average stress before reloading to calculate the yield surface. Let us consider the calculation of a yield surface corresponding to normal tension or compression along the X_2 direction (σ_{22}) combined with X_1-X_2 shearing (σ_{12}). The boundary conditions imposed are

$$\begin{aligned} &\dot{N}_{11} = \dot{N}_{23} = \dot{N}_{31} = \dot{N}_{32} = \dot{N}_{33} = 0 \\ &\frac{1}{2}\,(\dot{N}_{21} + \dot{N}_{12}) = \rho\dot{N}_{22} \\ &\dot{f}_{12} - \dot{f}_{21} = 0,\ \dot{f}_{31} = 0 \end{aligned} \qquad [26]$$

Loading is achieved by prescribing $\dot{f}_{22}$ and the stress ratio

Table II. Non-Schmid Factors for Ni_3Al at Several Temperatures

Temperature	Stress State	η_{ss}	η_{mm}	η_{zz}	η_{mz}	η_{sz}
	$\tau_{sm} > 0,\ \tau_{cb} > 0$	0	0.008	−0.008	0.008	−0.015
θ = 293 K	$\tau_{sm} < 0,\ \tau_{cb} < 0$	0	−0.008	0.008	−0.008	−0.015
	$\tau_{sm} > 0,\ \tau_{cb} < 0$	0	0.008	−0.008	0.008	0.014
	$\tau_{sm} < 0,\ \tau_{cb} > 0$	0	−0.008	0.008	−0.008	0.014
	$\tau_{sm} > 0,\ \tau_{cb} > 0$	0	0.036	−0.036	0.037	−0.065
θ = 600 K	$\tau_{sm} < 0,\ \tau_{cb} < 0$	0	−0.036	0.036	−0.037	−0.065
	$\tau_{sm} > 0,\ \tau_{cb} < 0$	0	0.030	−0.030	0.031	0.054
	$\tau_{sm} < 0,\ \tau_{cb} > 0$	0	−0.030	0.030	−0.031	0.054
	$\tau_{sm} > 0,\ \tau_{cb} > 0$	0	0.046	−0.046	0.048	−0.083
θ = 800 K	$\tau_{sm} < 0,\ \tau_{cb} < 0$	0	−0.046	0.046	−0.048	−0.083
	$\tau_{sm} > 0,\ \tau_{cb} < 0$	0	0.037	−0.037	0.038	0.067
	$\tau_{sm} < 0,\ \tau_{cb} > 0$	0	−0.037	0.037	−0.038	0.067

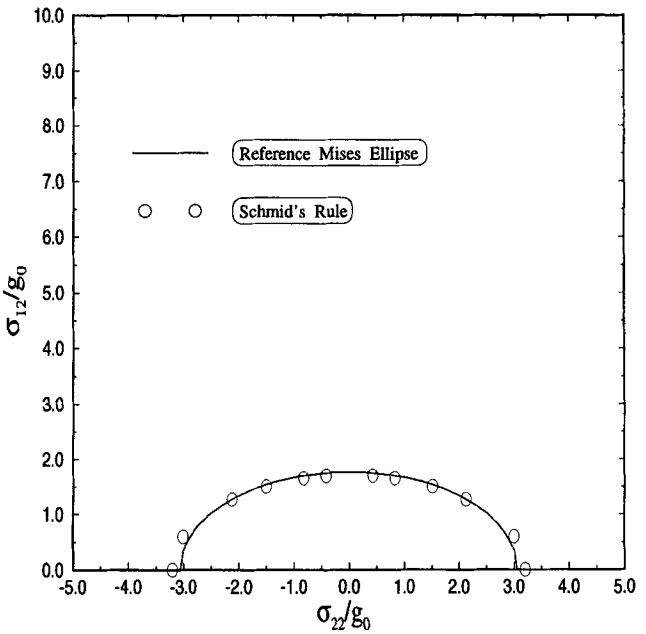

Fig. 3—Initial constant offset plastic strain yield surface constructed in the σ_{22}-σ_{12} section of stress space for an initially isotropic, unstrained polycrystal where Schmid's rule holds. The von Mises yield ellipse is constructed using the average Taylor factor 3.06 for uniaxial tension or compression of an isotropic polycrystal. The offset strain is 0.002.

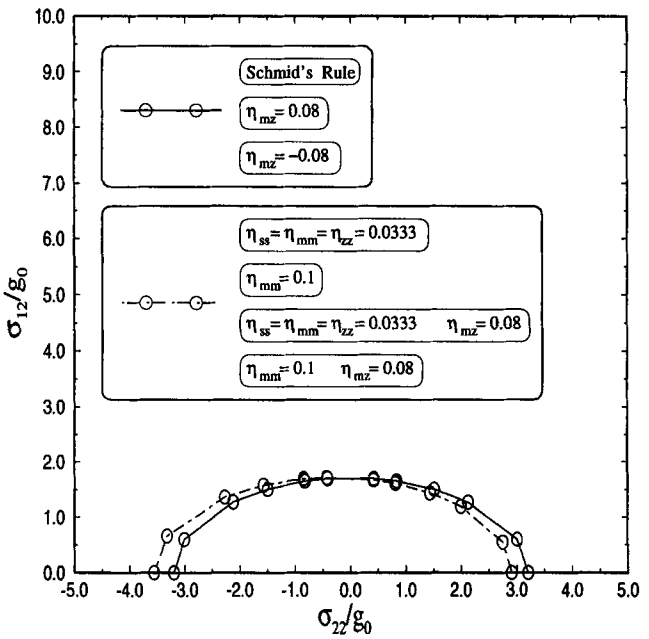

Fig. 4—Initial constant offset plastic strain yield surfaces constructed in the σ_{22}-σ_{12} section of stress space for an initially isotropic, unstrained polycrystal for Schmid's rule and for various non-Schmid effects. The offset strain is 0.002.

ρ, and

$$\mathbf{f} = \mathbf{F} \cdot \mathbf{F}_i^{-1} \qquad [27]$$

$$\mathbf{N} = \mathbf{F}_i \cdot \mathbf{n}/\det(\mathbf{F}_i) \qquad [28]$$

where $\mathbf{F}_i$ is the deformation gradient from the initial state to the unloaded state of zero average stress. By keeping track of the Mises effective plastic strain and varying the stress ratio ρ, constant offset effective plastic strain yield surfaces were constructed. An offset plastic strain of 0.002 was used in this study.

A total of 246 random oriented grains with fcc type slip systems were used. The slip system hardening is specified by taking g_α^0 to be the critical resolved shear stress g_0 for each slip system and by specifying $h(\gamma_a)$ in Eq. [11] to be

$$h(\gamma_a) = h_\infty + (h_0 - h_\infty)\ \mathrm{sech}^2\left\{\left(\frac{h_0 - h_\infty}{g_\infty - g_0}\right)\gamma_a\right\} \qquad [29]$$

The plastic hardening constants used are $g_\infty = 1.8g_0$, $h_0 = 8.9g_0$, and $h_\infty = 0$. These hardening values were obtained by fitting to the stress-strain data of Chang and Asaro[34] for the tensile deformation of Al-3 wt pct Cu single crystals along the ⟨211⟩ direction. The latent hardening ratio is taken as $q = 1.4$ for noncoplanar and $q = 1$ for coplanar slip systems. The crystal elastic constants are given as $C_{11} = 842g_0$, $C_{12} = 607g_0$, and $C_{44} = 377g_0$, where these constants fit the elastic anisotropy of copper single crystals. For a concise presentation, only nonzero non-Schmid factors are listed herein.

Figure 3 shows the initial constant offset plastic strain yield surface where Schmid's rule holds. The data points are shown against the reference Mises ellipse. The Mises ellipse is calibrated to a tensile yield stress of $3.06g_0$. The 0.002 offset surface is very close to the Mises ellipse, in agreement with the previous work of Hill[37] and Asaro and Needleman.[2]

Figure 4 shows initial constant offset plastic strain yield surfaces for Schmid's rule and for various non-Schmid effects. Since the three curves for Schmid's rule, $\eta_{mz} = 0.08$, and $\eta_{mz} = -0.08$ are hardly distinguishable from each other, only one curve is plotted to represent this group. The

situation is similar for the other four cases for $\eta_{ss} = \eta_{mm} = \eta_{zz} = 0.0333$, $\eta_{mm} = 0.1$, $\eta_{ss} = \eta_{mm} = \eta_{zz} = 0.0333$ with $\eta_{mz} = 0.08$, and $\eta_{mm} = 0.1$ with $\eta_{mz} = 0.08$; therefore, only one of these four nearly indistinguishable curves is plotted. It is noticed that there is virtually no difference between the cases for Schmid's rule, $\eta_{mz} = 0.08$, and $\eta_{mz} = -0.08$; there is no difference between the cases for $\eta_{ss} = \eta_{mm} = \eta_{zz} = 0.0333$ and $\eta_{ss} = \eta_{mm} = \eta_{zz} = 0.0333$ with $\eta_{mz} = 0.08$; and there is no difference between the cases for $\eta_{mm} = 0.1$ and $\eta_{mm} = 0.1$ with $\eta_{mz} = 0.08$. It is thus concluded that the non-Schmid effects associated with pure shear, *i.e.*, η_{mz}, will have no net influence by themselves on the initial yielding of the polycrystal aggregate. In Figure 4, the case for $\eta_{ss} = \eta_{mm} = \eta_{zz} = 0.0333$ is a simple Coulomb friction model, which corresponds to a pressure sensitivity factor of $\kappa = 0.1$; a strength differential effect is clearly seen on the polycrystal initial yield surface. For the case of $\eta_{mm} = 0.1$, which is a simple friction model for the slip, it is very interesting to find that the initial yield surface is virtually identical to that of $\eta_{ss} = \eta_{mm} = \eta_{zz} = 0.0333$, where a strength differential effect is also found. As they should, non-Schmid effects associated with hydrostatic stress will have some finite influence on the polycrystal initial yield surface and result in the strength differential effect. However, for a random oriented polycrystal, it is a bit surprising that no interactions are found between the non-Schmid effects associated with the pure shear stresses and the non-Schmid effects associated with hydrostatic stress in terms of the influence toward the initial constant offset yield surface. Here, it is stressed that an implicit assumption is made: non-Schmid factors will not change sign or magnitude with different stress states of each constituent single crystal. This is, in fact, the case with Ni_3Al single crystals, which are the origin for the single crystal tension-compression asymmetry. The case with Ni_3Al will be dealt with later in Section III–F.

C. *Stress-Strain Behavior*

In polycrystal materials, the stress-strain behavior is not only affected by the hardening function (including self- and latent hardening) but also by the texture development of the aggregate. In this section, material properties are the same as those described in Section B.

Figure 5(a) shows the Mises effective stress–effective strain curves for the case when the Schmid rule applies and for various cases when there are non-Schmid effects under uniaxial tension. At small strains, *i.e.*, $\varepsilon_e < 0.15$, the stress-strain curves are clustered into two groups: one group with non-Schmid effects associated with hydrostatic stress and the other group with Schmid's rule or without non-Schmid effects associated with hydrostatic stress; this is consistent with the results obtained in our initial yield surface study. As the strain gets larger, *i.e.*, $\varepsilon_e > 0.15$, the texture begins to form and the curves in each one of those two groups begin to separate from other curves within the same group. We note that a ⟨111⟩ fiber texture is forming along the tensile axis under uniaxial tension. If the tensile axis is along the [111] direction, then the slip systems that have the highest resolved shear stresses are $[011](11\bar{1})$, $[101](11\bar{1})$, $[101](\bar{1}11)$, $[110](\bar{1}11)$, $[110](1\bar{1}1)$, and $[011](1\bar{1}1)$ (Figure 5(b)). Note that the normals to the slip planes (marked by "**m**" in Figure 5(b)) have an angle of

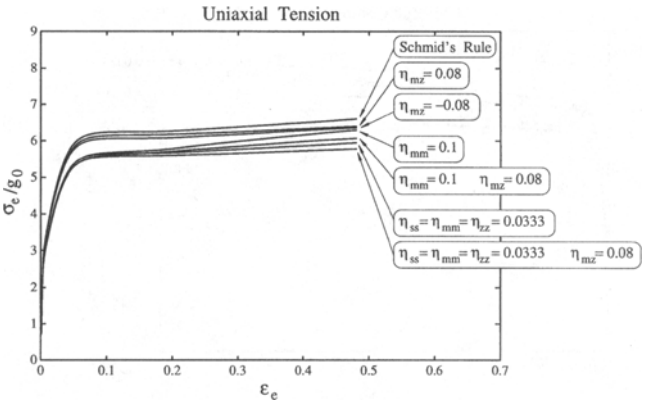

(*a*)

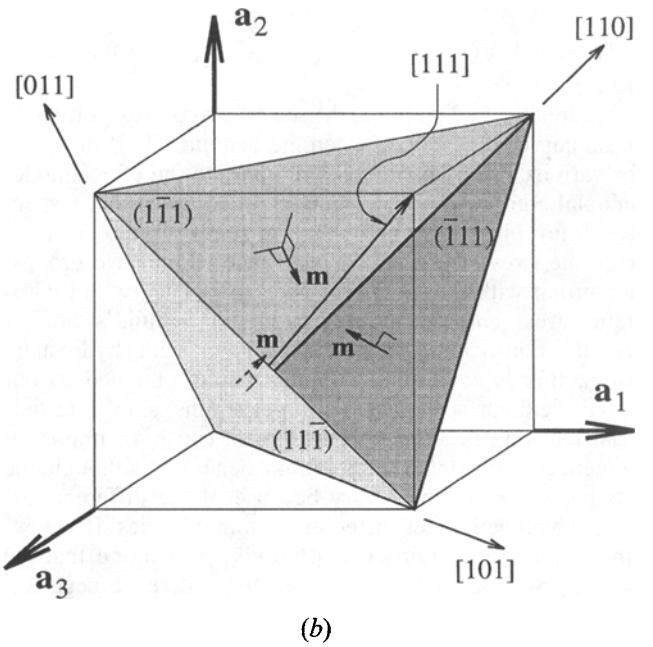

(*b*)

Fig. 5—(*a*) Mises effective stress–effective strain curves for the Schmid rule and for various non-Schmid effects, under uniaxial tension. (*b*) A single crystal under uniaxial tension along the [111] direction, where the slip systems that have the highest resolved shear stresses are $[011](11\bar{1})$, $[101](11\bar{1})$, $[101](\bar{1}11)$, $[110](\bar{1}11)$, $[110](1\bar{1}1)$, and $[011](1\bar{1}1)$. The normals to the slip planes are marked by **m**.

70.5 deg with the [111] direction which is much larger than 45 deg—the average angle between the tensile axis and the slip plane normals of a random oriented aggregate. Since now $\tau_{mm} = \sigma_{22} \cos^2 (70.5 \text{ deg}) = \sigma_{22}/9 << \sigma_{22}/2 = \sigma_{22} \cos^2 (45 \text{ deg})$, the influence of η_{mm} decreases as ⟨111⟩ fiber texture develops; this is the reason why the stress-strain curve for $\eta_{mm} = 0.1$ approaches that obtained with the Schmid rule. For the other cases, similar analyses can be applied to explain the stress-strain behavior under different non-Schmid factors. Nevertheless, under simple tension, the non-Schmid factor η_{mz}, whether positive or negative, tends to lower the global stress as the texture develops (*e.g.*, compare Schmid's rule with $\eta_{mz} = 0.08$ or -0.08; $\eta_{mm} = 0.1$ with $\eta_{mm} = 0.1$ plus $\eta_{mz} = 0.08$; and $\eta_{ss} = \eta_{mm} = \eta_{zz} = 0.0333$ with $\eta_{ss} = \eta_{mm} = \eta_{zz} = 0.0333$ plus $\eta_{mz} = 0.08$). While the reduced influence of friction η_{mm} may raise the global stress closer to the curve for Schmid's rule as the texture develops, the curve for Coulomb friction $\eta_{ss} = \eta_{mm}$

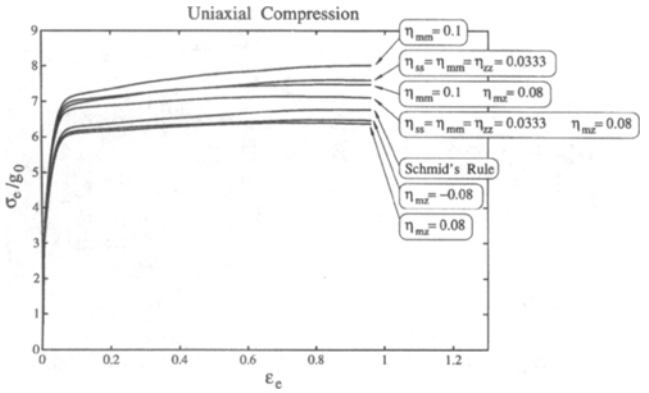

Fig. 6—Mises effective stress–effective strain curves for the Schmid rule and for various non-Schmid effects under uniaxial compression.

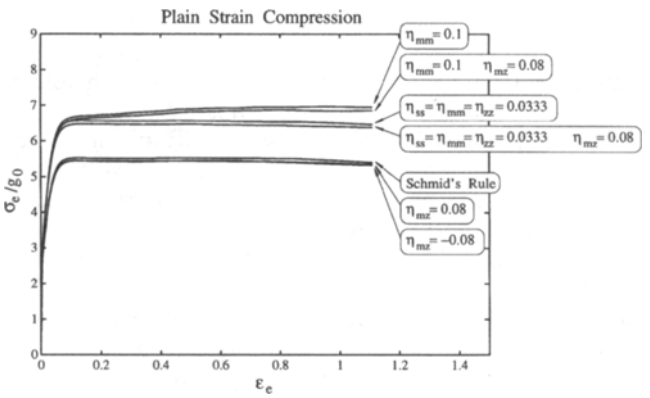

Fig. 7—Mises effective stress–effective strain curves for the Schmid rule and for various non-Schmid effects under plain strain compression.

$= \eta_{zz} = 0.0333$ is, as it should be, parallel to that obtained with Schmid's rule.

Figures 6 and 7 show the Mises effective stress–effective strain curves for the case when the Schmid rule applies and for various cases where there are non-Schmid effects under uniaxial compression and plain strain compression, respectively. For either loading history, at small strains, *i.e.*, $\varepsilon_e < 0.05$, the stress-strain curves are clustered into two groups: one group with non-Schmid effects associated with hydrostatic stress and the other group with Schmid's rule or without non-Schmid effects associated with hydrostatic stress; this is consistent with the results obtained in our initial yield surface study. At larger strains, similar to uniaxial tension, the texture development can have important influences toward the stress-strain behavior, although the relative influences may vary because of the different textures developed under different loading histories. If we examine the stress-strain curves closely, it is found that (1) the non-Schmid factor η_{mz}, whether positive or negative, tends to lower the global stress as the texture develops; (2) the Coulomb friction model is relatively orientation dependent and always results in a stress-strain curve parallel to that of Schmid's rule; and (3) unlike the Coulomb friction model, the simple friction model with $\eta_{mm} > 0$ is very sensitive to texture development, although there is no difference between these two models at the initial yielding.

D. *Texture Development*

Texture development is very prominent in large deformation processes in polycrystals. Since single crystal properties (mechanical, electrical, thermal, or magnetic) are often crystallographic dependent, it is important to accurately describe the deformation textures formed under different mechanical processing methods—wire drawing (uniaxial tension), forging (uniaxial compression), and rolling (plain strain compression). Again, the material properties used in this section are the same as those specified in Section B.

We denote the "laboratory" Cartesian axes by $\mathbf{e}_i$ and the cube crystal axes in grain K by $\mathbf{a}_i^{(K)}$; the loading axis $\mathbf{e}_2$ is taken to fall within the [100], [110], [111] standard stereographic triangle, as shown in Figure 8(a). Figure 8(b) shows the "inverse pole figure" of the loading axis $\mathbf{e}_2$, describing the random distribution of single crystal orientations of a polycrystal aggregate in the undeformed state.

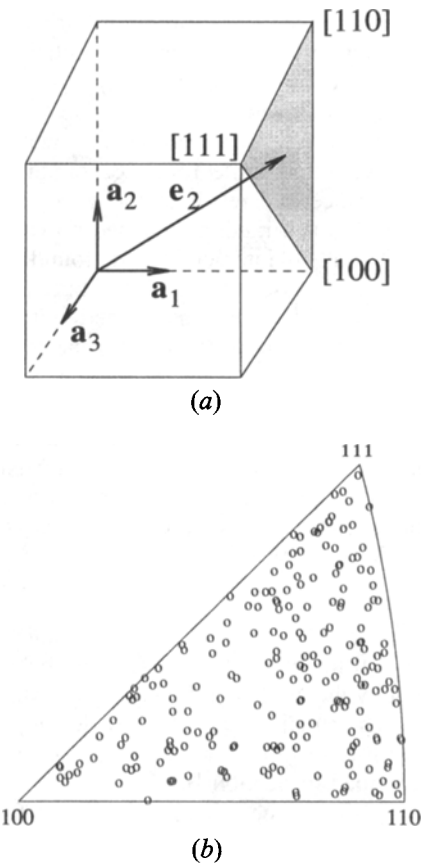

Fig. 8—(*a*) Unit cube used to describe crystallographic directions; the standard triangle with corners [100], [110], and [111] is used throughout to describe crystal directions in three dimensions; $\mathbf{e}_2$ corresponds to a unit vector along a material fiber parallel to the axis of tension or compression. (*b*) Inverse pole figure of the loading axis $\mathbf{e}_2$, describing the random distribution of single crystal orientations of a polycrystal aggregate in the undeformed state.

A total of 201 grains are used in this aggregate. This random distribution corresponds to a nearly isotropic aggregate.

Figure 9 shows the deformation textures in uniaxial tension for the Schmid rule or with different non-Schmid effects at an effective strain of $\varepsilon_e = 1.37$. A strong [111] texture along with a small gathering near [410] develops for all four cases shown. Comparing to Schmid's rule, the texture for the Coulomb friction model $\eta_{ss} = \eta_{mm} = \eta_{zz} =$

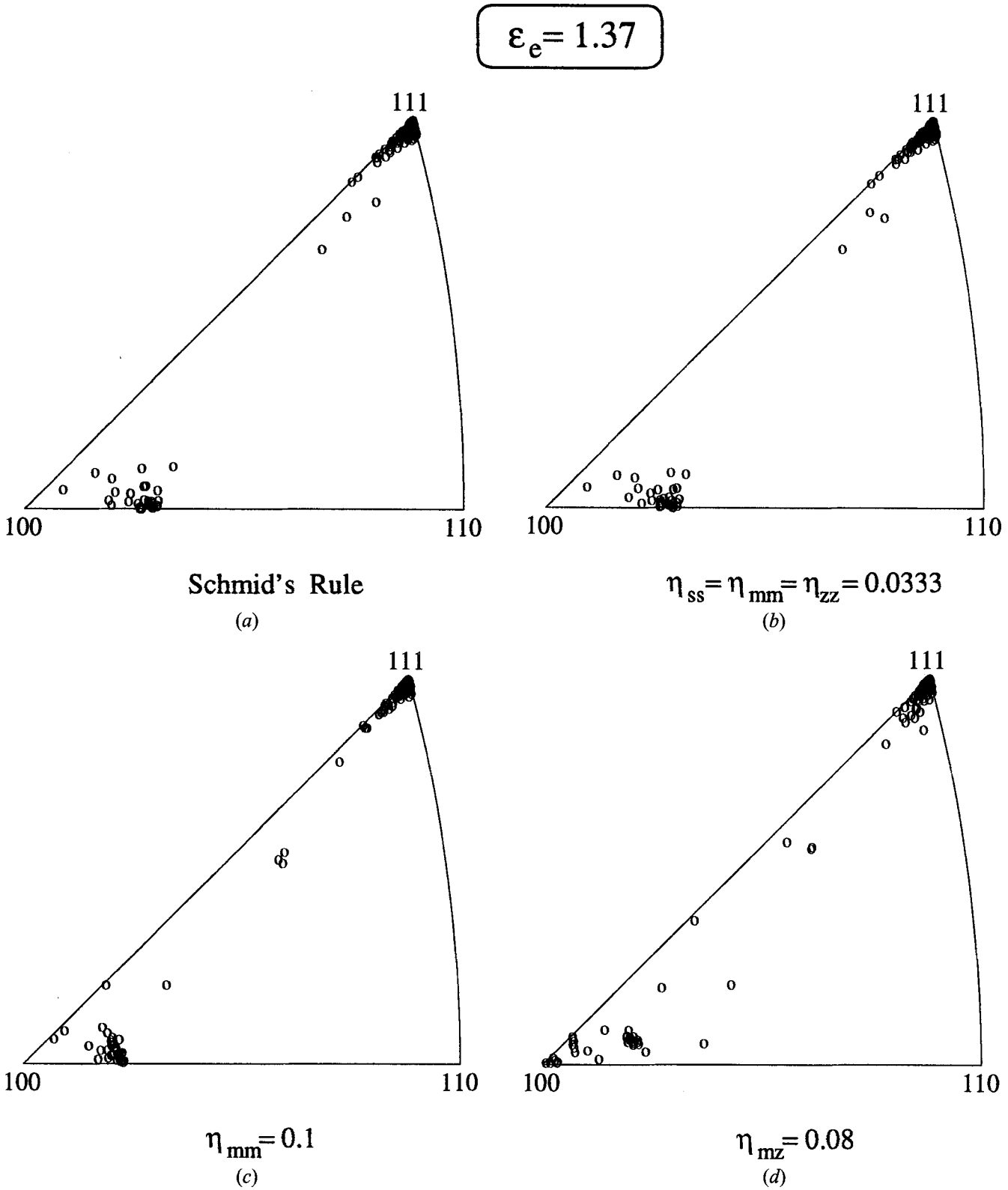

Fig. 9—(*a*) through (*d*) Deformation textures in uniaxial tension for the Schmid rule or with different non-Schmid effects at an effective strain of ε_e = 1.37.

0.0333 is virtually the same; while some minor differences are found for the friction model η_{mm} = 0.1 and for η_{mz} = 0.08—*i.e.*, the small cluster near [410] for η_{mm} = 0.1 is closer to [100] than that for Schmid's rule, and a third cluster near [100] appears for η_{mz} = 0.08.

Figure 10 shows the deformation textures in uniaxial compression for the Schmid rule or with different non-Schmid effects at an effective strain of ε_e = 0.96. At this strain level, all the major textures in Figure 10 are around the [631]-[441] line, although there are distinct differences between the Schmid rule and the friction model η_{mm} = 0.1 or η_{mz} = 0.08. Again, the texture for the Coulomb friction

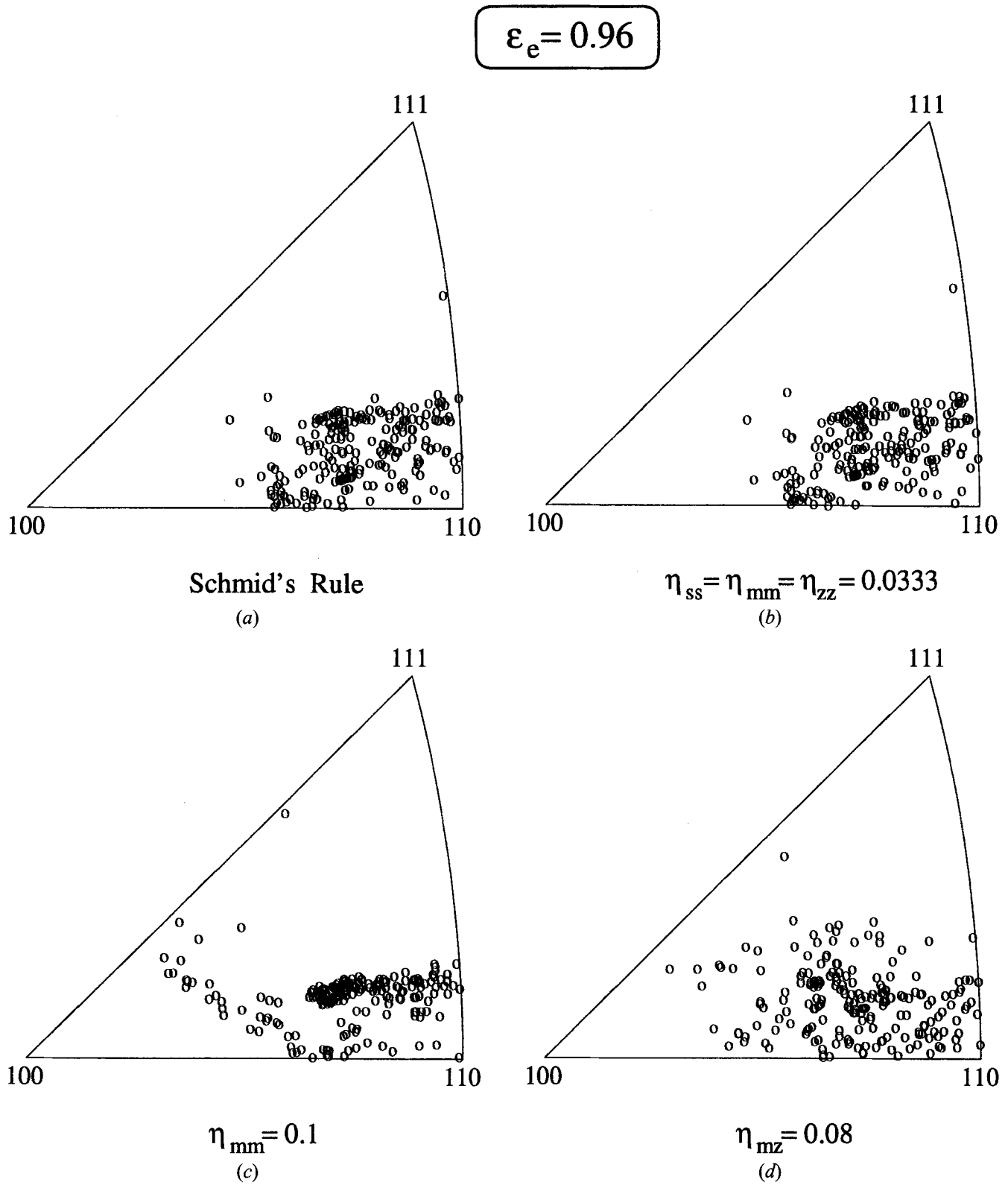

Fig. 10—(*a*) through (*d*) Deformation textures in uniaxial compression for the Schmid rule or with different non-Schmid effects at an effective strain of $\varepsilon_e = 0.96$.

model $\eta_{ss} = \eta_{mm} = \eta_{zz} = 0.0333$ is, as it should be, virtually the same as that for Schmid's rule, reflecting the orientation independence of the Coulomb friction model. With the Schmid rule and $\eta_{ss} = \eta_{mm} = \eta_{zz} = 0.0333$, the texture is found somewhat diffusely distributed between the [210]-[110] line and the [631]-[331] line; with the case of friction model $\eta_{mm} = 0.1$, the major texture component close to the [631]-[441] line is much sharper, and a secondary texture component is found around the [210]-[311] line; and with $\eta_{mz} = 0.08$, while the major texture component is similar to that for Schmid's rule, a lot of scattering around the major texture component is found.

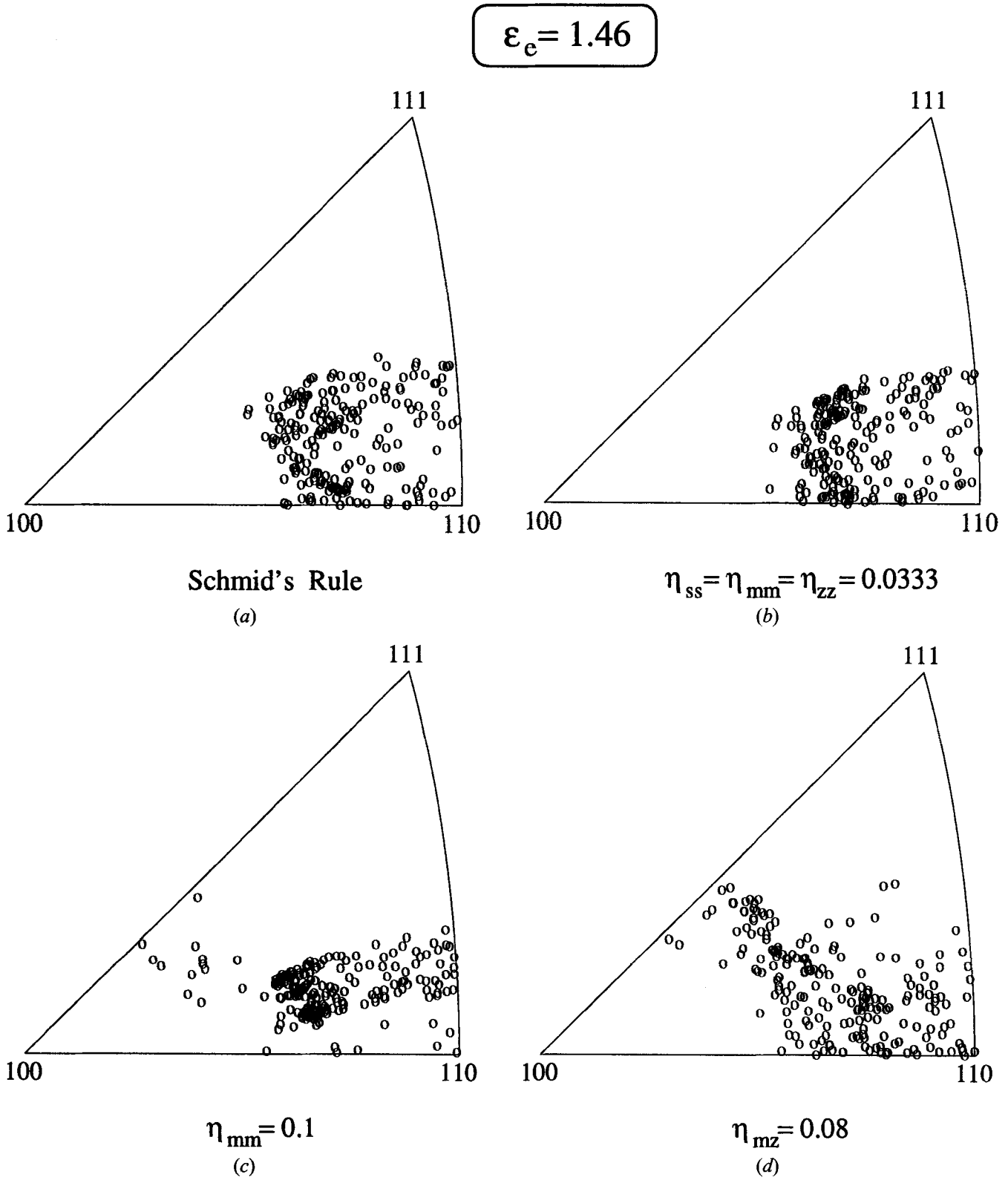

Fig. 11—(*a*) through (*d*) Deformation textures in uniaxial compression for the Schmid rule or with different non-Schmid effects at an effective strain of $\varepsilon_e = 1.46$.

Figure 11 shows the deformation textures in uniaxial compression for the Schmid rule or with different non-Schmid effects at an effective strain of $\varepsilon_e = 1.46$. At this stage (Figure 11), except that there is virtually no difference between Schmid's rule and the Coulomb friction model $\eta_{ss} = \eta_{mm} = \eta_{zz} = 0.0333$, the textures with non-Schmid effects are quite different than those with Schmid's rule, although their major texture components are still somewhat alike. With the Schmid rule and $\eta_{ss} = \eta_{mm} = \eta_{zz} = 0.0333$, the texture is found diffusely distributed around the [320]-[421]-[331] line; with the case of friction model $\eta_{mm} = 0.1$, the texture is distributed close to the [631]-[441] line with

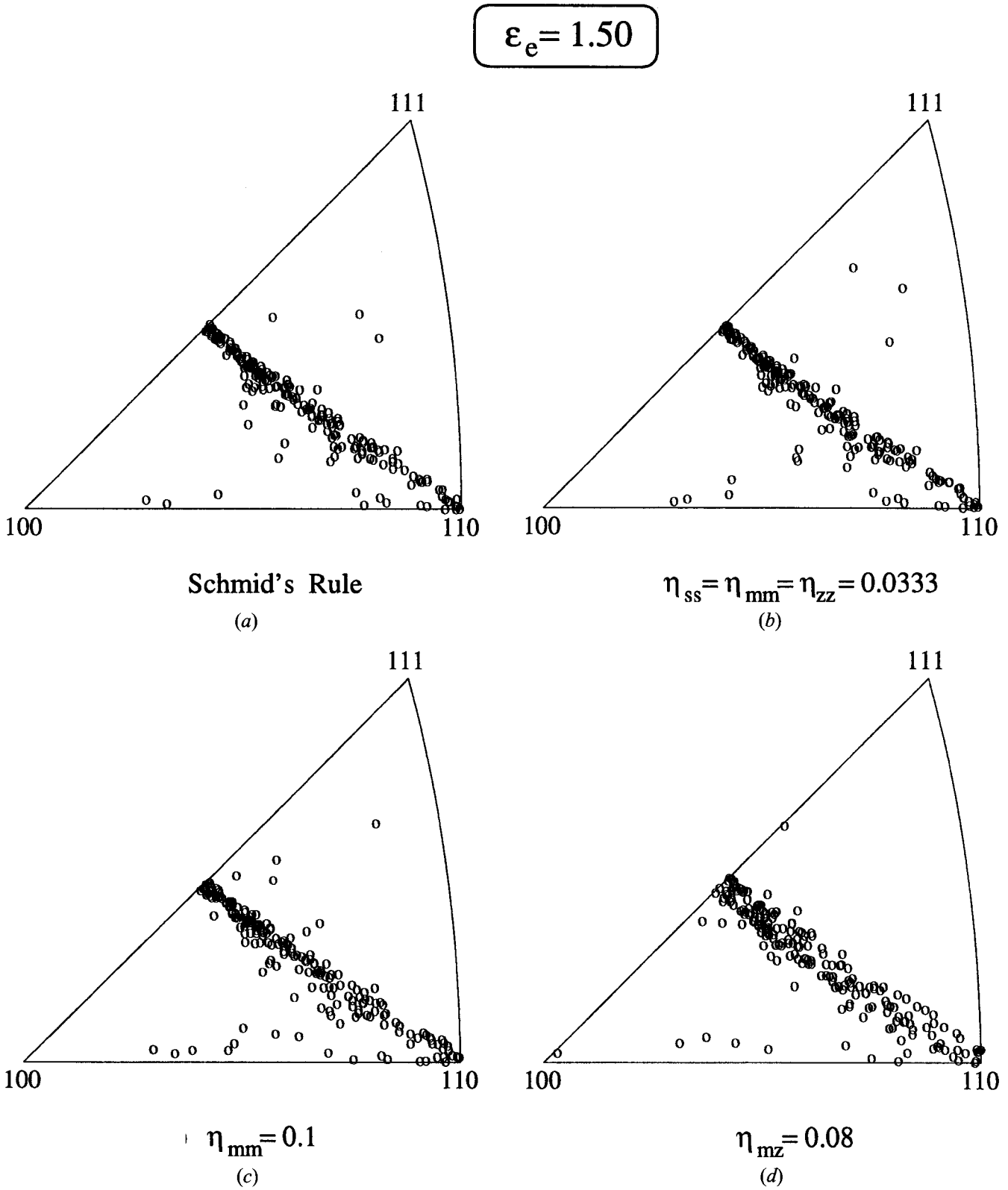

Fig. 12—(*a*) through (*d*) Deformation textures in plain strain compression for the Schmid rule or with different non-Schmid effects at an effective strain of $\varepsilon_e = 1.50$.

a heavy cluster near [631]; and with $\eta_{mz} = 0.08$, the major texture is distributed around the [430]-[311] line. The influence of non-Schmid effects on the details of the texture development found in this example shows the need for an accurate constitutive description for the non-Schmid behavior in crystalline solids. As demonstrated earlier, the details of texture development combined with the non-Schmid effects have significant influence on the stress-strain behavior. It is noted that comparing our Schmid's rule results to those obtained by Asaro and Needleman,[2] a more diffuse and a little different texture is developed; this is because the initial texture used in this study is randomly generated, while

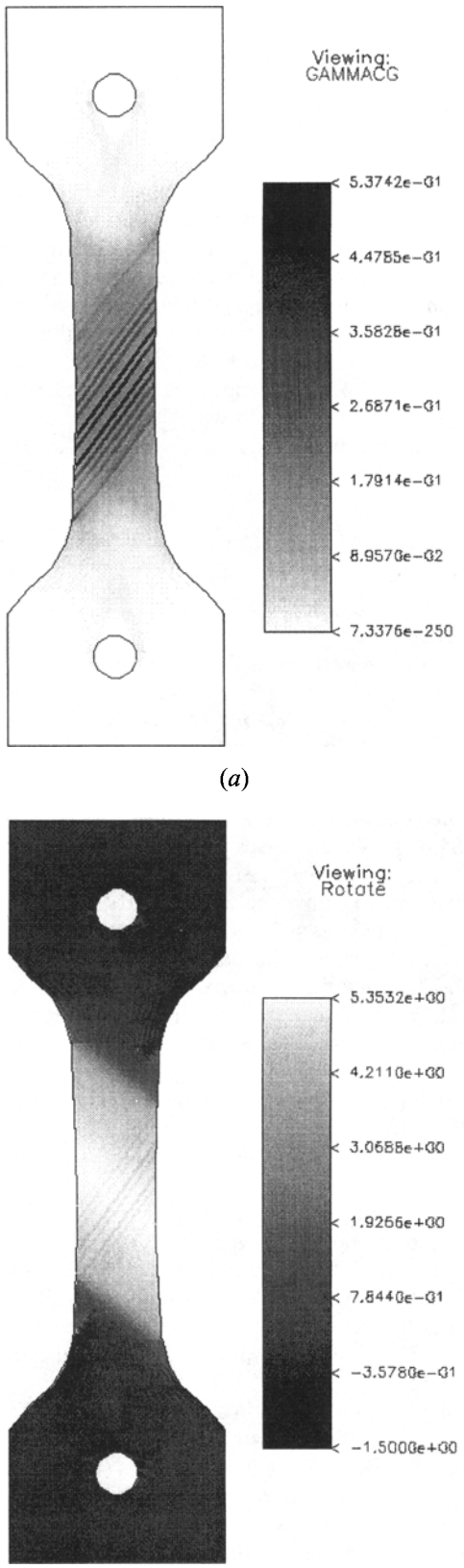

Fig. 13—Deformed crystal: (*a*) map of accumulated sum of slips; and (*b*) map of lattice rotation, measured in degrees toward the tensile axis from the original 10 deg tilt (positive values show counterclockwise rotation). η_{ss} = 0.08 at a nominal tensile strain of 0.10. Figure taken from Dao and Asaro.[27]

in Asaro and Needleman's research, the initial texture was introduced by uniformly distributing crystal orientations within the standard triangle.

Figure 12 shows the deformation textures in plain strain compression for the Schmid rule or with different non-Schmid effects at an effective strain of ε_e = 1.50. The texture developed is along the [110]-[311] line for all four cases, with virtually no difference between them.

E. *Localized Deformation and Texture*

While in Taylor-like models deformation within a constituent single crystal of a polycrystal aggregate is assumed to be uniform, in reality, this is not the case. It is now realized that nonuniform deformation modes like necking and shear banding are entirely natural, inevitable outcomes of finite deformation of ductile crystalline materials.[1,12,13,14,27,28] Whether the non-Schmid effects can have significant influence on the shear localizations in polycrystals and therefore have further influence on the texture development remains a question to be answered. To answer this question, we will first examine the localized deformation and nonuniform lattice rotations in single crystals.

1. *Localized deformation in single crystals*

Localized deformation modes like necking and shear banding are found to be natural consequences of finite deformation of single crystals. Shear bands, for example, form within defect-free single crystals that display positive hardening in both single slip and multiple slip modes (*e.g.*, Asaro,[13] Peirce *et al.*,[14] Dao and Asaro[1,27]).

Dao and Asaro[1,27] found that moderate non-Schmid effects can significantly increase the critical hardening rate for shear band initiation and intensify the shear bands (*i.e.*, larger strains can accumulate within the shear band at the same global strain level). For the formation of macroscopic shear bands (MSBs), *geometrical softening* induced by nonuniform lattice rotations plays a major role whether the Schmid rule holds (Asaro[13] and Peirce *et al.*[14]) or there exist some non-Schmid effects (Dao and Asaro[1,27]). Dao and Asaro[27] confirmed that coarse slip bands (CSBs) can form under a significant hardening rate with some moderate non-Schmid effects that are well within the range estimated in Section A.

While non-Schmid effects do have important influences on the localization process in single crystals, we would naturally expect non-Schmid effects to play a big role in the localization in polycrystals as well. To answer the question of whether the CSBs and the MSBs can affect the texture development in polycrystals, it is intuitive to examine the nonuniform lattice rotations caused by the formation of CSBs and MSBs. Dao and Asaro[27] performed a number of finite element simulations in single crystals studying the CSBs and their transition to MSBs. The plastic properties used are the same as those specified in Section B, except that 2-D double slip model was used.[27] Figure 13(a) shows a map of the accumulated sum of slips and Figure 13(b) a map of the lattice rotation, measured in degrees toward the tensile axis from the original 10 deg tilt, at an engineering strain of 0.10. The coarse slip pattern is clear and there is no apparent necking (Figure 13(a)); these bands are closely aligned with the active slip systems. Figure 13(b), a map of lattice rotation, shows that the lattice mismatch across the CSBs is very small (less than 2 deg). Figure 14(a)

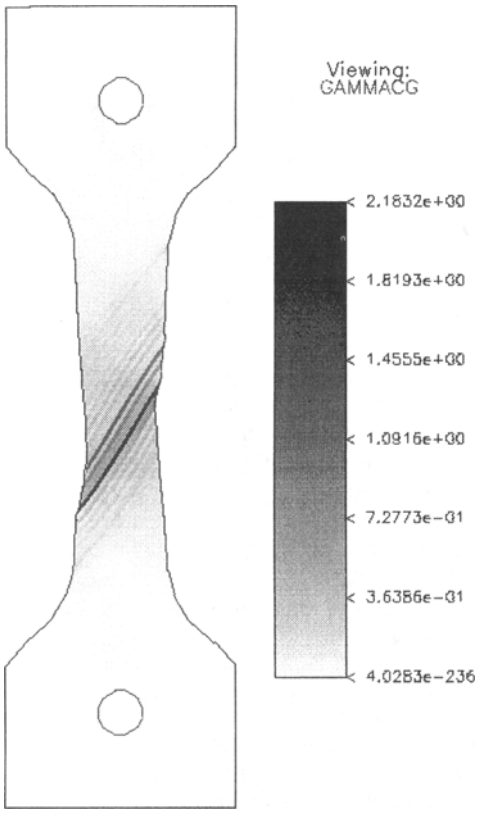

(*a*)

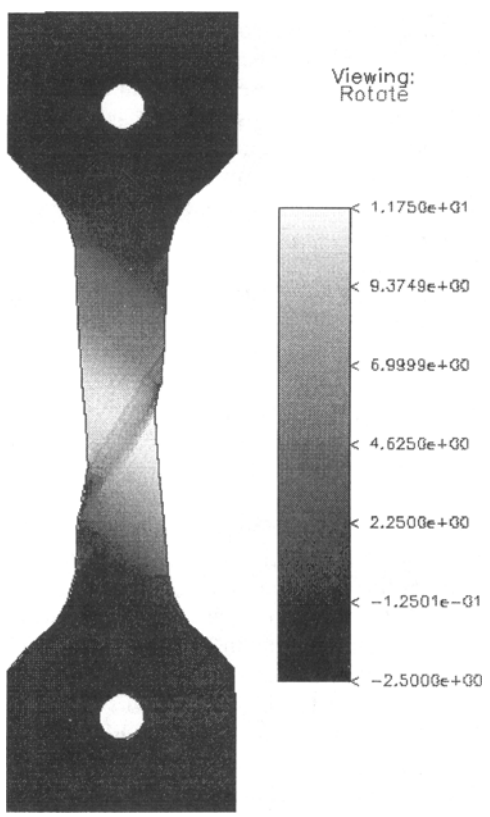

(*b*)

Fig. 14—Deformed crystal: (*a*) map of accumulated sum of slips; and (*b*) map of lattice rotation, measured in degrees toward the tensile axis from the original 10 deg tilt; positive values show counterclockwise rotation. $\eta_{ss} = 0.08$ at a nominal tensile strain of 0.16. Figure taken from Dao and Asaro.[27]

shows a map of the accumulated sum of slips, and Figure 14(b) a map of the lattice rotation, measured in degrees toward the tensile axis from the original 10 deg tilt, at 0.16 engineering strain. The MSB is very well developed at this stage (Figure 14(a)), and the MSB is found to be misoriented about 5 deg from slip system $\mathbf{s}_1$ of the surrounding lattice. The lattice inside the MSB is rotated away from the surrounding lattice by about 5 to 7 deg (Figure 14(b)). It was noticed that if there were no non-Schmid effects, there were no CSBs in the calculations, although the MSBs formed in much the same way as described in the case where there existed non-Schmid effects (Dao and Asaro[27]). Now, from Figures 13(b) and 14(b), it is concluded that in single crystals, CSBs do not result in significant nonuniform lattice rotations while MSBs do. Therefore, it seems appropriate to expect that the CSB type of shear bands in polycrystals have little to do with the texture development, while the MSB type of shear bands may have some appreciable influences.

2. *Non-Schmid effects and localized deformation in polycrystals*

To study the localized deformation in polycrystals, any model that assumes uniform deformation within each of the constituent single crystals is inadequate. Therefore, the finite element model described in Section II–B–2 will be used.

The material hardening properties are the same as given in Section B: $g_\infty = 1.8g_0$, $h_0 = 8.9g_0$, and $h_\infty = 0$ in Eq. [29]. A simple Taylor hardening is taken with the latent hardening ratio $q = 1$. Isotropic elasticity is used with the Lame's constant $\lambda = 576.92g_0$ and the elastic shear moduli $G = 384.62g_0$, which corresponds to Young's modulus $E = 1000g_0$ and Poisson's ratio $\nu = 0.3$. Finally, the reference shear rate is taken as $\dot{a} = 0.001\ \text{s}^{-1}$, and the rate sensitivity is given as $m = 0.005$. One calculation is done using Schmid's rule, while the other calculation is performed with only the nonzero non-Schmid factor $\eta_{ss} = 0.07$. Both runs are under plain strain compression.

Figures 15(a) and (b) show the contour maps of the accumulated sum of slips (γ_a) at a true strain of $\varepsilon = -0.223$ for the Schmid rule and $\eta_{ss} = 0.07$, respectively; and Figures 15(c) and (d) show the contour maps of the rate of the accumulated sum of slips ($\dot{\gamma}_a$) at a true strain of $\varepsilon = -0.223$ for the Schmid rule and $\eta_{ss} = 0.07$, respectively. From Figures 15(a) and (b), the deformation apparently starts to get localized in both cases with Schmid's rule and the non-Schmid factor $\eta_{ss} = 0.07$, although the peak strain with non-Schmid effects $\eta_{ss} = 0.07$ is more than 50 pct larger than that of the Schmid rule. At this early stage, shear bands in Figure 15(a) (Schmid's rule) are more diffuse than those in Figure 15(b) ($\eta_{ss} = 0.07$). This trend can be seen more clearly in Figures 15(c) and (d). In Figure 15(c) (Schmid's rule), we can see that $\dot{\gamma}_a$ (a measure of overall deformation rate) is highly localized, with some areas (full white) almost nondeforming at the moment; several SE-NW and SW-NE MSBs are forming across the whole sample. In Figure 15(d) ($\eta_{ss} = 0.07$), features similar to those in Figure 15(c) (Schmid's rule) are found, although (1) the peak $\dot{\gamma}_a$ is almost 50 pct larger, (2) the localization is more concentrated compared to the relatively diffuse looking bands found in Figure 15(c) (Schmid's rule), and (3) there are several grains exhibiting the coarse slip pattern, *i.e.*, grains 2, 25, and 26, while in the corresponding grains in Figure 15(c) (Schmid's

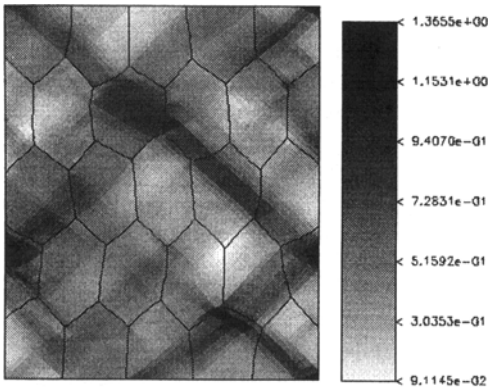

γ_a at $\varepsilon = -0.223$ (Schmid's Rule)

(*a*)

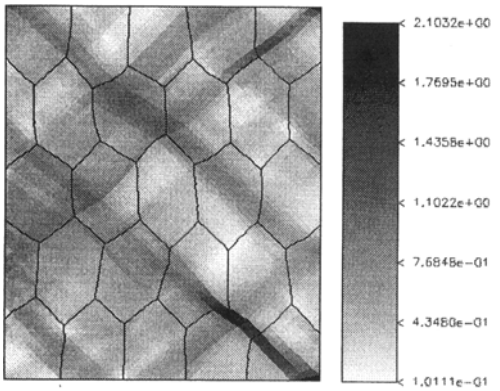

γ_a at $\varepsilon = -0.223$ ($\eta_{ss} = 0.07$)

(*b*)

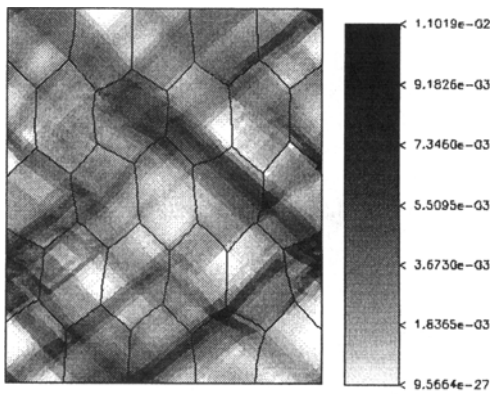

$\dot{\gamma}_a$ at $\varepsilon = -0.223$ (Schmid's Rule)

(*c*)

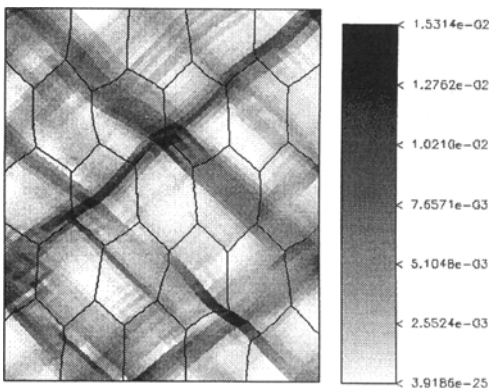

$\dot{\gamma}_a$ at $\varepsilon = -0.223$ ($\eta_{ss} = 0.07$)

(*d*)

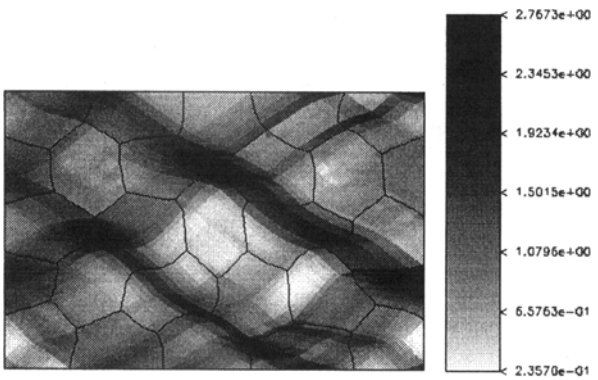

γ_a at $\varepsilon = -0.511$ (Schmid's Rule)

(*e*)

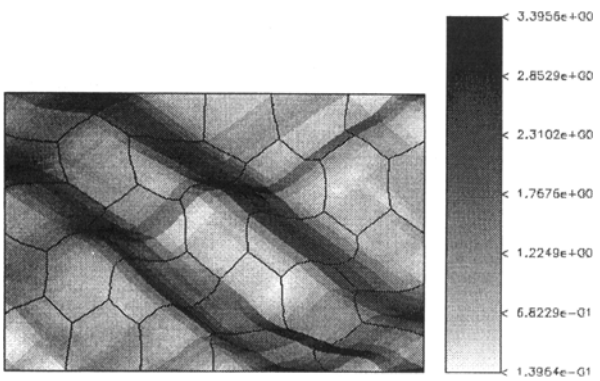

γ_a at $\varepsilon = -0.511$ ($\eta_{ss} = 0.07$)

(*f*)

Fig. 15—(*a*) through (*f*) Development of localized deformation in the model polycrystal. Comparisons are made between the case of Schmid's rule and the case with non-Schmid effects $\eta_{ss} = 0.07$.

rule), no such features can be found. At a true strain of $\varepsilon = -0.511$, Figures 15(e) and (f) show the contour maps of the accumulated sum of slips (γ_a) for the Schmid rule and $\eta_{ss} = 0.07$, respectively. At this stage, the MSBs in Figures 15(e) (Schmid's rule) and (f) ($\eta_{ss} = 0.07$) are both fully developed; peak γ_a in Figure 15(f) ($\eta_{ss} = 0.07$) is found to be 23 pct larger than that in Figure 15(e) (Schmid's rule).

Figure 16 shows the γ_a *vs* compressive strain plot. It is evident that peak γ_a for $\eta_{ss} = 0.07$ is always higher than that for the case of Schmid's rule. Note that the biggest increase for $\eta_{ss} = 0.07$ happens between 0.1 and 0.2 true strain, and afterward, those two curves are practically parallel; this shows the strong influence of the non-Schmid effects toward the shear band initiation.

3. *Influences on texture development*

Harren and Asaro[3] have shown that with Schmid's rule, the Taylor model is very good in terms of calculating de-

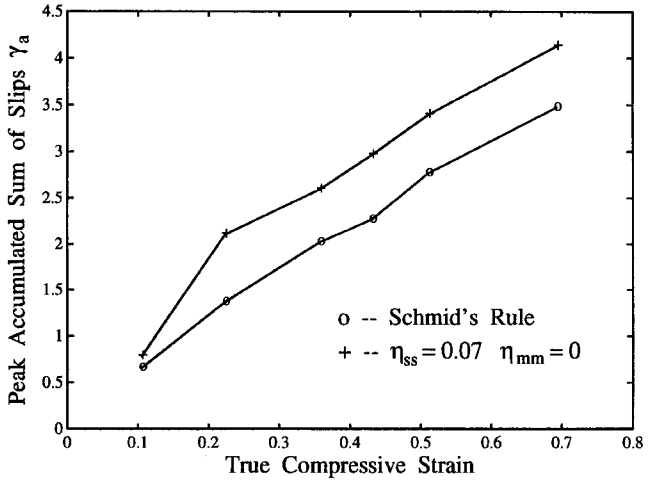

Fig. 16—Accumulated sum of slips γ_a *vs* compressive strain plot.

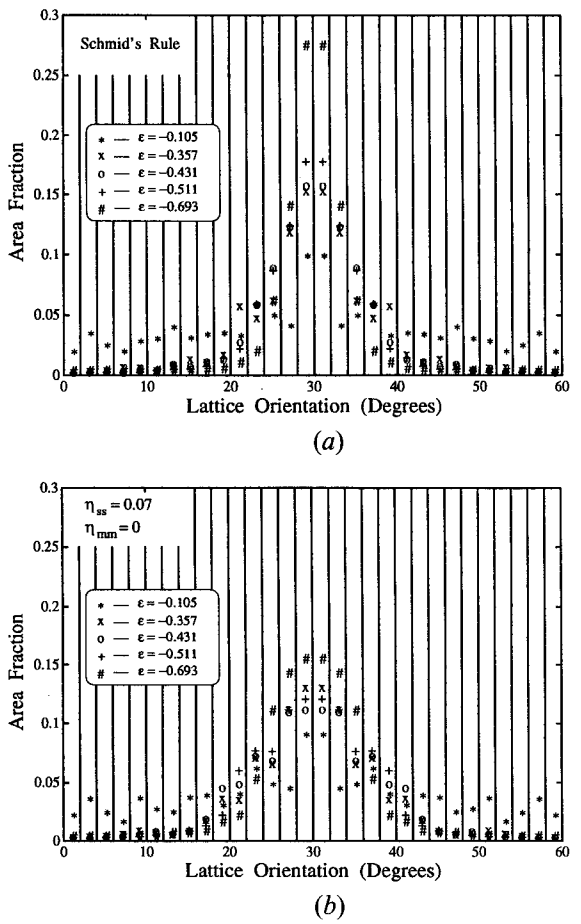

Fig. 17—Texture development of the 2-D model polycrystal for (*a*) the Schmid rule and (*b*) $\eta_{ss} = 0.07$.

formation textures, although the texture predicted by the Taylor model is much sharper than that calculated using the finite element model where localized deformation is rigorously modeled. Here, we study the influences of non-Schmid effects, and the non-Schmid effects induced heavier shear banding toward the deformation texture. The two cases studied are the same as those in Section 2, where Schmid's rule holds in one case and $\eta_{ss} = 0.07$ is given as the non-Schmid factor in the other case.

To describe texture in this 2-D idealized polycrystal model, we specify the following. The lattice at each point in the polycrystal aggregate (actually, in each constant strain triangle finite element) has its initial orientation 0 deg $\leq \psi <$ 60 deg, as described in Figure 2(a). In the deformed state, let ψ stand for the current lattice orientation at each point; ψ will still be within 0 deg $\leq \psi <$ 60 deg or an appropriate material symmetry operation will be applied to bring it within 0 deg $\leq \psi <$ 60 deg. In order to represent this distribution of initial or deformed crystal orientations, the interval of 0 deg $\leq \psi <$ 60 deg is broken up into 30 subintervals: 0 deg $\leq \psi <$ 2 deg, 2 deg $\leq \psi <$ 4 deg, . . . , 58 deg $\leq \psi <$ 60 deg. Associated with each of these subintervals is the volume fraction (area fraction indeed with this idealized polycrystal model) of the aggregate that has the lattice orientation within the subinterval. As discussed by Harren and Asaro,[3] the ideal texture orientation (ITO) under compression is 30 deg.

Figures 17(a) and (b) show the texture development for the Schmid rule and $\eta_{ss} = 0.07$, respectively. In Figure 17(a) (Schmid's rule), the texture progressively sharpens as the global strain gets larger. It is interesting to observe the "texture saturation" within the strain range between $\varepsilon = -0.357$ and $\varepsilon = -0.511$. In Figure 17(b) ($\eta_{ss} = 0.07$), the texture, in general, sharpens as the deformation gets larger. The similar texture saturation also happens within the strain range between $\varepsilon = -0.357$ and $\varepsilon = -0.511$, although there is some small "detexturization" going on within this period where the peak texture intensity drops from $\varepsilon = -0.357$ to $\varepsilon = -0.431$ before picking up again from $\varepsilon = -0.431$ to $\varepsilon = -0.511$. The occurrence of texture saturation and especially "detexturization" demonstrates that heavy shear banding can reorient its surrounding slowly deforming lattice, which can delay the texturization toward the ITO and result in much less pronounced texture.

F. *Applications to Ni_3Al*

Simple applications to Ni_3Al polycrystals with respect to initial yielding, stress-strain behavior, and texture development are dealt with using the Taylor-like model described earlier. After carefully examining existing experimental data in the literature, especially those obtained by Umakoshi *et al.*,[38] the magnitude of non-Schmid effects between room temperature and 77 K is found to be appreciable although smaller compared to that at elevated temperatures. The constants listed in Table II are thus rather conservative ones, especially for room temperature. One also notices that the orientation dependencies for Ni_3Al are the same, except with different magnitudes (*i.e.*, magnitude becomes larger as temperature goes higher) at different temperatures below the octahedral slip to cubic slip transition temperature.

In this section, moderate non-Schmid factors (corresponding to the 600 K data in Table II) and relatively large non-Schmid factors (corresponding to the 800 K data in Table II) are applied to compare with the results obtained assuming Schmid's rule. The non-Schmid factors introduced here have the exact orientation dependence for each constituent single crystal, as observed experimentally (Figure 18). The objective here is to see the influence of the non-Schmid effects; therefore, except the varying non-Schmid factors, the elastic and plastic properties are fixed using room temperature properties. The elasticity con-

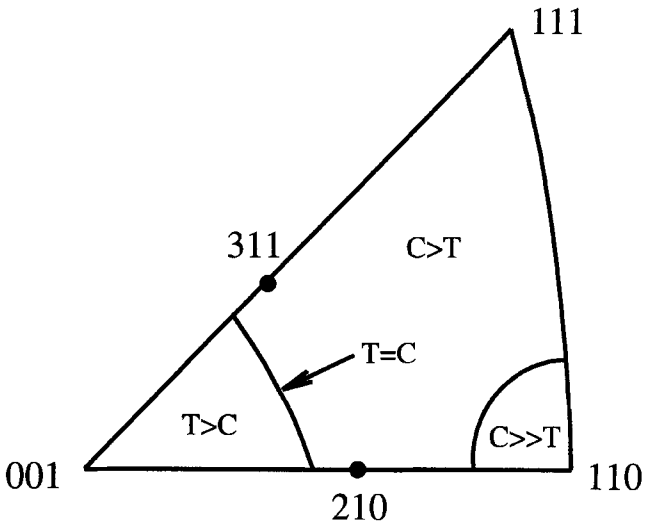

Fig. 18—Summary of tension/compression asymmetry in a Ni_3Al single crystal,[39] where "T" stands for tension and "C" stands for compression.

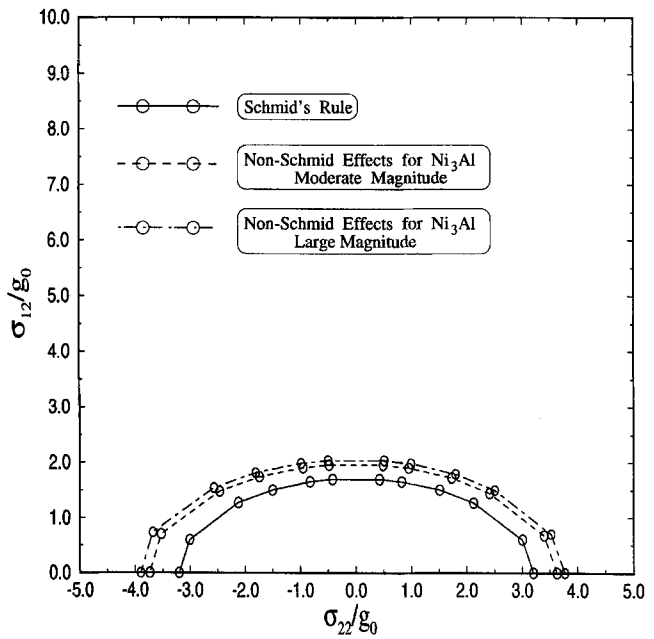

Fig. 19—Initial constant offset plastic strain yield surfaces constructed in the σ_{22}-σ_{12} section of stress space for an initially isotropic, unstrained polycrystal for Schmid's rule, moderate non-Schmid factors, and large non-Schmid factors. The offset strain is 0.002.

stants are given as C_{11} = 223 GPa, C_{12} = 148 GPa, and C_{44} = 125 GPa (Yoo[40]). The plastic properties are given as g_0 = 45 MPa with a simple linear hardening h = 300 MPa in Eq. [11]. The latent hardening ratios q = 1.4 for noncoplanar and q = 1 for coplanar slip systems are used.

1. *Initial yielding*

Figure 19 shows the initial constant offset plastic strain yield surfaces using Schmid's rule, moderate non-Schmid factors (corresponding to the 600 K data in Table II), and large non-Schmid factors (corresponding to the 800 K data in Table II). One prediction from the initial yield surfaces calculated in Figure 19 is that there is practically no strength differential effect for Ni_3Al isotropic polycrystal aggregates, although single crystal Ni_3Al may display some

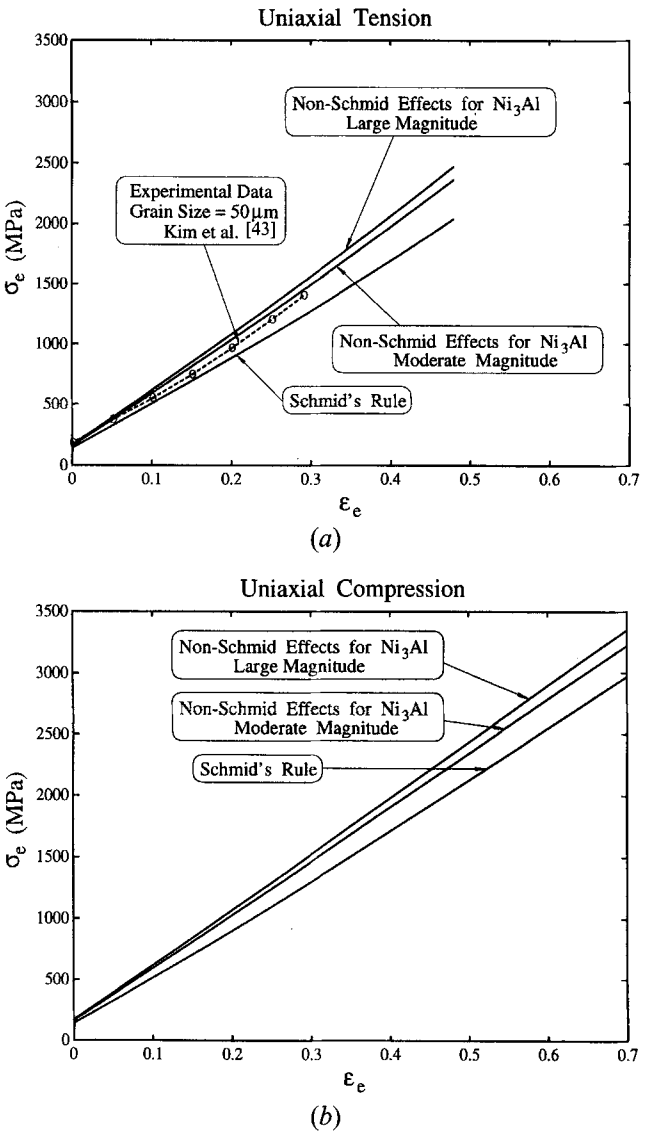

Fig. 20—Calculated effective stress–effective strain curves under (*a*) uniaxial tension and (*b*) uniaxial compression.

large tension-compression asymmetry. The initial yield surfaces for Ni_3Al polycrystals with moderate to large non-Schmid factors are "fatter" versions of those with Schmid's rule (or reference Mises ellipse). We define the generalized polycrystal Taylor factor as

$$\bar{m} = | \sigma_{22} | / g_0 \qquad [30]$$

where $|\sigma_{22}|$ is the absolute value of the global stress under uniaxial loading along the X_2 axis and g_0 is the critical resolved shear stress when all other stress components are zero. It is noted that under Schmid's rule, the definition (Eq. [30]) agrees with the traditional Taylor factor definition as in Gil Sevillano *et al.*[41] and Tomé *et al.*[42] Generalized polycrystal Taylor factors much higher than 3.06 are observed for the two cases with the kind of non-Schmid effects in Ni_3Al shown in Figure 18.

2. *Stress-strain behavior*

Figures 20(a) and (b) show the calculated effective stress-strain curves under uniaxial tension and uniaxial compression, respectively. From Figure 20(a), we see that the calculated stress-strain curves compare fairly well to the

experimental data points measured by Kim *et al.*,[43] although a simple linear hardening is used. For either tensile or compressive loading, the calculated strain hardening for Ni_3Al is very high, about 3800 MPa if we assume Schmid's rule and around 4500 MPa if we use non-Schmid effects as input. One important observation from the calculated curves is that the kind of non-Schmid behavior of Ni_3Al single crystals shown in Figure 18 can significantly raise the strain hardening, whether the polycrystal aggregate is under tension or compression. For isotropic fcc polycrystals, the simple relation

$$\partial\sigma_{22} / \partial\varepsilon = \bar{m}^2 \, \partial\tau / \partial\gamma \qquad [31]$$

is often used to connect the polycrystal aggregate behavior to that of the individual crystal, where $\partial\sigma_{22}/\partial\varepsilon$ is the hardening rate for a polycrystal under uniaxial loading, $\partial\tau/\partial\gamma$ is the shear hardening rate for the constituent single crystals, and $\bar{m}$ is the Taylor factor. For isotropic fcc polycrystals, $\bar{m} = 3.06$ is expected. Substituting $\partial\tau/\partial\gamma = 300$ MPa into Eq. [31], we find the apparent Taylor factor $\bar{m} \approx 3.5$ for Schmid's rule and $\bar{m} \approx 3.9$ for non-Schmid effects. The first increase to about 3.5 for the case of Schmid's rule is due to the high latent hardening, while the further increase to about 3.9 for the case with non-Schmid effects shows significant influence on hardening due to the non-Schmid effects. Intermetallic compounds such as Ni_3Al often show unusually high and almost constant hardening rates.[6,44,45] Schulson[44] applied Eq. [31] to estimate the Taylor factor $\bar{m}$ in Zr_3Al (a $L1_2$ intermetallic compound having very similar mechanical properties as Ni_3Al) and found that $\bar{m}$ may be as high as 5.5, which is much higher than 3.06 (average Taylor factor for isotropic fcc crystals). High latent hardening is suggested for Ni_3Al, where Aoki and Izumi[46] observed significant overshooting in single crystals. Our results suggest that non-Schmid effects and the high latent hardening may act together, resulting in the unusual hardening rate in polycrystalline intermetallics, consistent with available experimental evidence.

3. *Texture development*

The textures under uniaxial tension are found to be typical for fcc polycrystals with non-Schmid effects and with Schmid's rule, although an extra small concentration can be found near [100] for non-Schmid effects, similar to that found earlier in Figure 9(d) for $\eta_{mz} = 0.08$. Typical copper-type plain strain compression texture is also found for the cases of Schmid's rule and different Ni_3Al non-Schmid effects.

Figure 21 shows the textures under Schmid's rule and two different magnitudes of Ni_3Al non-Schmid effects at an effective strain of 0.95. Although the major texture components for all three cases are somewhat similar, the distinct differences between them are evident. With Schmid's rule, the major texture component is diffusely distributed between the [210]-[110] line and the [631]-[331] line. While with non-Schmid effects, the major component is densely clustered near the [841] orientation, with some secondary scatters along the [841]-[441] line and the [210]-[311] line. From this example, it is clear that non-Schmid effects may have distinct influences toward the texture development.

4. *Localized deformation and texture*

As shown in Section E, non-Schmid effects can enhance strain localization in polycrystals and slow the texture development. Thus, the Taylor-like model we used may not be applicable or at least not accurate if there is heavy shear banding.

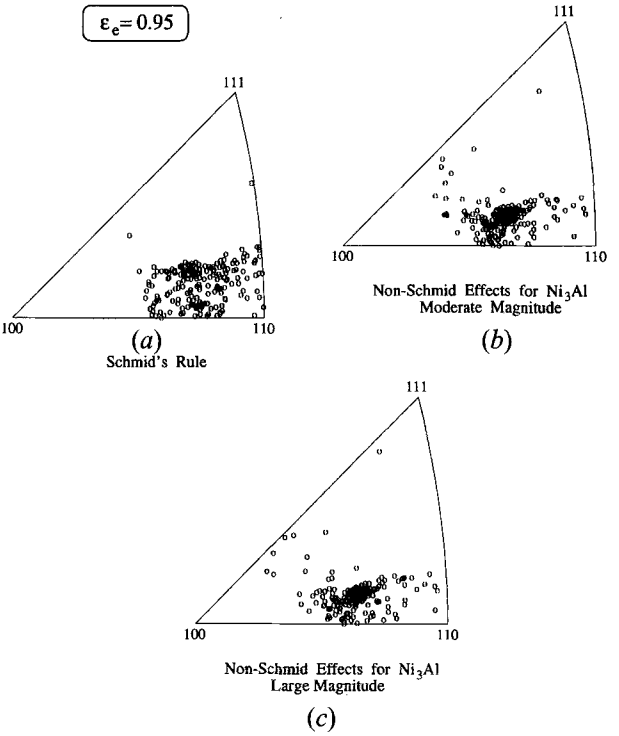

Fig. 21—(*a*) through (*c*) Deformation textures under Schmid's rule and two different magnitudes of Ni_3Al non-Schmid effects at an effective strain of 0.95.

In fact, consistent with the findings here in this study, Ball *et al.*[47] reported that very heavy shear banding does appear for coarse-grained Ni_3Al polycrystal under rolling and develops a strong brass-type texture component, while less pronounced shear banding occurs for fine-grained Ni_3Al polycrystal and a typical copper-type texture develops under rolling. Heavy shear banding was suggested to be the reason for the texture differences between the coarse and fine grain size samples. Ball *et al.* also concluded that heavy shear banding could result in less pronounced textures, which agrees with our findings in Section E. A large grain size relative to the sample size may also result in the sample becoming a "multicrystal aggregate" instead of a "true polycrystal aggregate."

From the results obtained in Section E and existing experimental evidence, it is clear that for the Taylor-like models to be accurate, there are two requirements: (1) the sample must be a true polycrystal aggregate, and (2) there should be no heavy shear banding in the sample.

IV. DISCUSSION AND CONCLUSIONS

In this article, we have studied the influences of non-Schmid effects on the mechanical behavior of polycrystals. A Taylor-like model and a finite element model were used, where arbitrarily large deformation and the accompanying large lattice rotation were rigorously accounted for. To summarize the results for polycrystals obtained in Section III, we conclude the following.

1. Non-Schmid effects related to hydrostatic stress have important influences on polycrystal initial yielding, while non-Schmid factors related to pure shear do not.
2. Non-Schmid effects can significantly affect the polycrystal stress-strain behavior by changing the strain hardening rate, and the influence on the rate of strain hardening may be enhanced by the texture development except for the case where deviations from Schmid's rule are purely of a Coulomb friction type.
3. Except for the Coulomb friction model, non-Schmid effects can have distinct influence on texture development, especially under uniaxial compression.
4. Non-Schmid effects may significantly affect the localization process in polycrystals, in that sharper and more intensive shear banding is expected for polycrystals with non-Schmid effects.
5. Heavy shear banding is found to produce less pronounced textures, consistent with existing experimental evidence on Ni_3Al.
6. The kind of non-Schmid effects existing in Ni_3Al can increase the generalized Taylor factor to values much higher than 3.06, raise the polycrystal strain hardening rate much higher than that which would be obtained using Schmid's rule, and influence the deformation texture.

The results presented in this study clearly show that non-Schmid effects can have significant influence on the polycrystal mechanical behavior. In materials like intermetallic compounds, crystalline polymers, and perhaps many hcp materials, where non-Schmid effects are often found to be significant, accurate constitutive descriptions incorporating non-Schmid effects may be necessary to predict the polycrystal mechanical behavior.

ACKNOWLEDGMENTS

This work was supported by the National Science Foundation under Contract No. DMR91-10930. Computations were performed at the San Diego Supercomputer Center. The authors gratefully acknowledge helpful discussions with Drs. Said Ahzi and Ming Li during the course of this study.

REFERENCES

1. M. Dao and R.J. Asaro: *Mater. Sci. Eng. A*, 1993, vol. 170, pp. 143-60.
2. R.J. Asaro and A. Needleman: *Acta Metall.*, 1985, vol. 33, pp. 923-53.
3. S.V. Harren and R.J. Asaro: *J. Mech. Phys. Solids*, 1989, vol. 37, pp. 191-232.
4. J.A. Barendreght and W.N. Sharpe, Jr.: *J. Mech. Phys. Solids*, 1973, vol. 21, pp. 113-23.
5. S. Takeuchi and E. Kuramoto: *Acta Metall.*, 1973, vol. 21, pp. 415-25.
6. K. Aoki and O. Izumi: *Acta Metall.*, 1978, vol. 26, pp. 1257-63.
7. Y. Minonishi: *Phil. Mag. A*, 63 (1991) 1085-93.
8. Z. Bartczak, R.E. Cohen, and A.S. Argon: *Macromolecules*, 25 (1992) 4692-4704.
9. G.I. Taylor: *J. Inst. Met.*, 62 (1938) 307-25.
10. G.I. Taylor: in *Stephen Timoshenko 60th Anniversary Volume*, J.M. Lessels, ed., Macmillan, New York, NY, 1938, pp. 218-24.
11. R. Hill and J.R. Rice: *J. Mech. Phys. Solids*, 20 (1972) 401-13.
12. R.J. Asaro and J.R. Rice: *J. Mech. Phys. Solids*, 25 (1977) 309-38.
13. R.J. Asaro: *Acta Metall.*, 27 (1979) 445-53.
14. D. Peirce, R.J. Asaro, and A. Needleman: *Acta Metall.*, 31 (1983) 1951-76.
15. Q. Qin and J.L. Bassani: *J. Mech. Phys. Solids*, 40 (1992) 813-33.
16. Q. Qin and J.L. Bassani: *J. Mech. Phys. Solids*, 40 (1992) 835-62.
17. R. Hill: *J. Mech. Phys. Solids*, 13 (1965) 213-22.
18. J.W. Hutchinson: *Proc. R. Soc. London A*, 319 (1970) 247-72.
19. T. Iwakuma and S. Nemat-Nasser: *Proc. R. Soc. London A*, 394 (1984) 87-120.
20. S. Nemat-Nasser and M. Obata: *Proc. R. Soc. London A*, 407 (1986) 343-75.
21. A. Molinari, G.R. Canova, and S. Ahzi: *Acta Metall.*, 35 (1987) 2983-94.
22. S.V. Harren: *J. Mech. Phys. Solids*, 1991, vol. 39, pp. 345-60.
23. S.V. Harren: *J. Mech. Phys. Solids*, 39 (1991) 361-83.
24. S.R. Kalidindi, C.A. Bronkhorst, and L. Anand: *J. Mech. Phys. Solids*, 40 (1992) 537-69.
25. K.K. Mathur and P.R. Dawson: *Int. J. Plast.*, 5 (1989) 67-94.
26. V. Paidar, D.P. Pope, and V. Vitek: *Acta Metall.*, 32 (1984) 435-48.
27. M. Dao and R.J. Asaro: *Scripta Metall.*, 30 (1994) 791-96.
28. D. Peirce, R.J. Asaro, and A. Needleman: *Acta Metall.*, 30 (1982) 1087-1119.
29. P.E. McHugh, R.J. Asaro, and C.F. Shih: *Acta Metall.*, 41 (1993) 1461-76.
30. T.-Y. Wu, J.L. Bassani, and C. Laird: *Proc. R. Soc. London A*, 435 (1991) 1-19.
31. J.L. Bassani and T.-Y. Wu: *Proc. R. Soc. London A*, 435 (1991) 21-41.
32. H. Dève, S. Harren, C. McCullough, and R.J. Asaro: *Acta Metall.*, 36 (1988) 341-65.
33. S.V. Harren, H.E. Dève, and R.J. Asaro: *Acta Metall.*, 36 (1988) 2435-80.
34. Y.W. Chang and R.J. Asaro: *Acta Metall.*, 29 (1981) 241-57.
35. R.J. Asaro: *Adv. Appl. Mech.*, 23 (1983) 1-115.
36. W.A. Spitzig, R.J. Sober, and O. Richmond: *Acta Metall.*, 23 (1975) 885-93.
37. R. Hill: *J. Mech. Phys. Solids*, 15 (1967) 79-95.
38. Y. Umakoshi, D.P. Pope, and V. Vitek: *Acta Metall.*, 32 (1984) 449-56.
39. D.P. Pope and S.S. Ezz: *Int. Met. Rev.*, 29 (1984) 136-67.
40. M.H. Yoo: in *High-Temperature Ordered Intermetallic Alloys II*, N.S. Stoloff, C.C. Koch, C.T. Liu, and O. Izumi, eds., Materials Research Society, Pittsburgh, PA, 1987, pp. 207-12.
41. J. Gil Sevillano, P. van Houtte, and E. Aernoudt: *Prog. Mater. Sci.*, 25 (1980) 69-409.
42. C. Tomé, G.R. Canova, U.F. Kocks, N. Christodoulou, and J.J. Jonas: *Acta Metall.*, 1984, vol. 32, pp. 1637-53.
43. M.S. Kim, S. Hanada, S. Watanabe, and O. Izumu: *Trans. JIM*, 29 (1988) 274-83.
44. E.M. Schulson: *Int. Met. Rev.*, 29 (1984) 195-209.
45. T.P. Weihs, V. Zinoviev, D.V. Viens, and E.M. Schulson: *Acta Metall.*, 35 (1987) 1109-18.
46. K. Aoki and O. Izumi: *Trans. JIM*, 19 (1978) 145-51.
47. J. Ball, B. Zeumer, and G. Gottstein: *Textures and Microstructures*, 1991, vols. 14–18, pp. 653-58.